

The Emergence of Halide Layered Double Perovskites

Brenda Vargas,[§] Germán Rodríguez-López,[§] and Diego Solis-Ibarra*



Cite This: *ACS Energy Lett.* 2020, 5, 3591–3608



Read Online

ACCESS |



Metrics & More

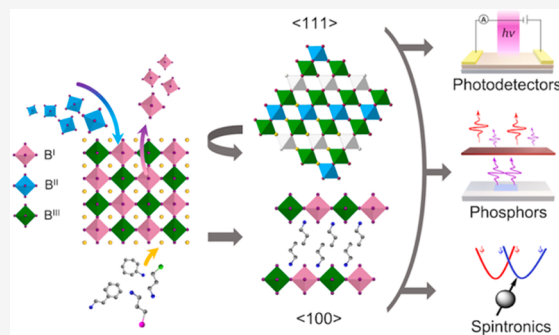


Article Recommendations



Supporting Information

ABSTRACT: Halide double perovskites have allowed the significant expansion of the possible metals and oxidation states in halide perovskites. Further, they have shown some remarkable properties and applications. Akin to the dimensional reduction in halide perovskites to generate layered perovskites, it has recently been shown that it is also possible to dimensionally reduce double perovskites to generate layered double perovskites (LDPs). The implications of such realization are tremendous from several different perspectives. First, it widens the space of possible metals, as LDPs can be made of B^I, B^{II}, and B^{III} cations and their permutations. Second, it allows the modulation of the materials' electronic structure through dimensional reduction and quantum confinement effects. Third, it allows the incorporation of many more organic cations, thereby providing a more chemically, structurally, and electronically diverse pool of materials. The combinations of these three factors result in a potentially infinite family of new materials with new or improved properties and applications. Herein, we describe the emergence of this new family and the known chemical, structural, and electronic features and review their proved and potential applications. Finally, we highlight some of the challenges and propose some future avenues of research and areas of opportunity for these materials.



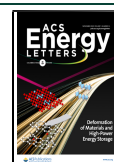
Over the past decade, lead halide perovskites have shown superb optical and electronic properties that have catapulted them to the forefront of photovoltaics and optoelectronics research. In photovoltaics, perovskite solar cells have rapidly increased their efficiency to a whopping 25.5%,¹ whereas in the optoelectronic field, they have rapidly found their way into lasers,² transistors,^{3,4} detectors,⁵ and photocatalysts,⁶ to name a few. While the optoelectronic properties of lead halide perovskite are outstanding,^{7,8} their stability and toxicity are serious concerns toward the commercialization of devices made from them. On the one hand, lead halide perovskites have shown to be sensitive to moisture and light exposure,⁹ and while significant strides have been made in this respect, there is still significant concern regarding the long-term stability of these materials and their devices. On the other hand, the presence of lead, which also happens to be highly bioavailable in these materials,¹⁰ is still a controversial issue in the field. For both reasons, since the early perovskite days, there has been a significant interest in exploring new materials to pursue more environmentally friendly and stable alternatives. Further, the exploration of other families of halide perovskites is also of interest because of the additional or alternative properties that could lead to new applications.

From the materials perspective, two of the main strategies to address the toxicity and stability issues are (a) substitution of lead for more benign elements and (b) dimensional reduction to improve the stability of the materials. The first approach to replace lead was to look for homovalent substitutions, such as Sn^{II} or Ge^{II},^{11,12} to obtain perovskites with the general formula AB^{II}X₃, where A is a monocation (e.g. Cs, methylammonium (MA), or formamidinium (FA)) and X a halide (Cl, Br, or I). Both metals, mainly tin, have produced decent solar cells with efficiencies of up to 13.2%.¹³ While these metals are significantly less toxic than lead, they have the added disadvantage of being oxygen-sensitive, with both metals being oxidized to Sn^{IV} or Ge^{IV} in the presence of O₂. Despite significant progress in recent years, particularly with the use of two-dimensional (2D) tin-halide perovskites¹⁴ and surface passivation,^{15,16} the lagging conversion efficiency and lack of stability are still serious concerns for this type of material. Other alternatives for the homovalent replacement of lead have

Received: August 31, 2020

Accepted: October 9, 2020

Published: October 29, 2020



been tried, albeit with minimal success.¹⁷ Perhaps the more significant limitation for homovalent substitution is the limited amount of B^{II} metals that are both reasonably stable in such an oxidation state and capable of forming three-dimensional perovskite structures.

An alternative to broaden the possible elements to replace lead is the use of halide double perovskites (also known as elpasolites), in which two metallic cations are combined to yield an “average” charge resembling that of traditional perovskites. For example, by combining one B^I and one B^{III} cation, one could obtain a double perovskite with general formula $A_2B^IB^{III}X_6$. In other words, one would replace two B^{II} metallic cations with one B^I and one B^{III} ($2 + 2 = 1 + 3$; or $2 B^{II} = B^I + B^{III}$). By doing this, the oxidation state restriction is somewhat lifted and the number of possible materials increases even more, not only because new elements can be incorporated but also because now the permutations are viable alternatives. To date, there are plenty of known halide double perovskites,¹⁸ some of which have shown remarkable properties and potential for photovoltaics and optoelectronic applications.¹⁹

To address the issue of stability on lead halide perovskites, one of the first and most successful strategies has been the use of 2D or 2D/3D hybrid perovskites as the absorber material.^{20,21} These materials incorporate large and generally hydrophobic layers²² between the perovskite inorganic layers. Consequently, the materials tend to be significantly more stable to water and light, at the expense of a somewhat reduced absorption, carrier mobility, and power conversion efficiency (PCE). To date, the most efficient 2D and 2D/3D perovskite solar cells have a PCE of 18.2 and 22.0%, respectively,²³ with operational stabilities of over a year.²⁴ Besides the improvement in stability provided by the inclusion of an organic cation, 2D perovskites allow the incorporation of a more diverse set of cations, which in turn makes these materials incredibly diverse, thereby offering plenty of opportunities to modify and tune their properties.²⁵ For example, one could further increase their hydrophobicity by including hydrophobic cations in their structure such as fluorinated aryl- or alkyl-amines; alternatively, one could further improve their absorption and conductivity by incorporating a conducting polymer in the layered perovskite.²⁶ Besides their application as solar cell absorbers, the dimensional reduction of lead halide perovskite results in materials with interesting optoelectronic properties that arise from electronic confinement within the inorganic layers.^{27,28} This electronic configuration is usually termed a quantum well structure, which endows these materials with enhanced exciton binding energies,²⁹ leading to favorable properties for their use as phosphors and emitters in LEDs,³⁰ for lasing,³¹ and as photodetectors.³²

More recently, heterovalent substitution and dimensional reduction have converged into a new family of materials: layered double perovskites or LDPs. Halide LDPs can be considered as the two-dimensional version of halide double perovskites or the double-metal version of layered perovskites (Figure 1). Either way, LDPs have further opened the chemical and structural diversity because now, metals in 1+, 2+, and 3+ oxidation states can be used and together with the vast number of possible cations, both organic and inorganic, create an infinite number of permutations. Further, dimensional reduction can generate profound changes in the material's electronic structure, as has been demonstrated for transition metal dichalcogenides.³³ From the first report of a mixed metal

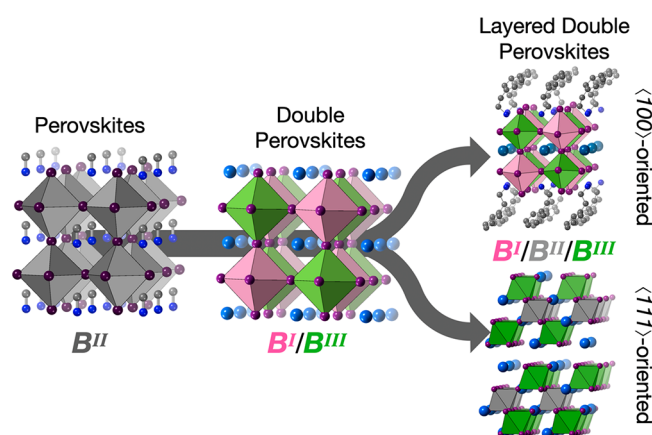


Figure 1. Schematic representation of the evolution from halide perovskites, to double perovskites, and finally to the resulting $\langle 100 \rangle$ and $\langle 111 \rangle$ -oriented perovskites upon dimensional reduction of double perovskites.

LDP in 2017,³⁴ the field has seen remarkable growth, and to date, there are well over 40 experimentally confirmed LDPs and many more computationally proposed. Herein, we provide an overview of the progress on the rational design of halide LDPs, by both computational and experimental efforts, their synthesis, and their electronic structure. Then, we will review some of the notable, proven, and potential applications of LDPs and conclude by summarizing some of the challenges and areas of opportunity in the field.

Halide LDPs can be considered as the two-dimensional version of halide double perovskites or the double-metal version of layered perovskites.

Classification and Structure. Halide LDPs can be classified similarly to conventional layered perovskites, with the more general classification based on the nature of the inorganic layers and, more precisely, in the relationship of the inorganic layers with the canonical 3D perovskite structure. Thus, LDPs can be divided into three general categories: $\langle 100 \rangle$, $\langle 110 \rangle$, and $\langle 111 \rangle$ depending on the direction of the imaginary cut needed to generate those layers (Figure 2). Their respective formulas would consequently be $A'_4A_{2n-2}B_n^{III}X_{6n+2}$ (for $\langle 100 \rangle$), $A'_4A_{2m}B_m^{III}X_{6m+4}$ (for $\langle 110 \rangle$) and $A'_2A_{q-1}B_{q-2}^{III}B_2^{III}X_{3q+3}$ (for $\langle 111 \rangle$), where A' and A represent monovalent cations and X represent a halide. Note that for these materials to be layered (2D), their respective n , m , and q values should be equal or

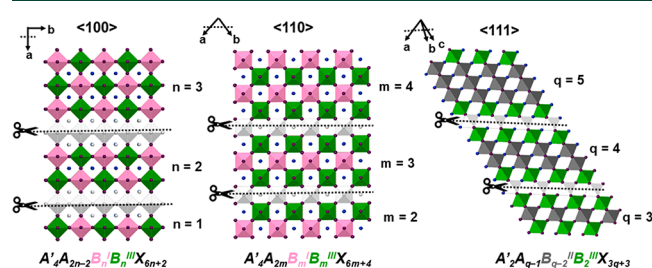


Figure 2. Schematic representation of cuts along the $\langle 100 \rangle$, $\langle 110 \rangle$, and $\langle 111 \rangle$ directions of the parent perovskite structure that give rise to the three families of layered double perovskites.

greater than 1, 2, and 3, respectively, as lower values yield lower-dimensional materials.

Of these three possible families of LDPs, only the $\langle 100 \rangle$ - and $\langle 111 \rangle$ -oriented LDPs have been experimentally demonstrated, while the $\langle 110 \rangle$ family has yet to be discovered. Also, for the purpose of this Focus Review, for the $\langle 111 \rangle$ -oriented family, we focused on those made of B^{II} and B^{III} metallic cations, as those are the only ones that have been experimentally obtained. However, it has been proposed and computationally validated that $\langle 111 \rangle$ -oriented LDPs made of B^{II} and B^{IV} metals yielding the general formula $A_4B_2^{\text{II}}B^{\text{IV}}X_{12}$ can be stable.³⁵ While the potential to also include metals in a 4+ oxidation state is extremely promising, experimental confirmation has not yet been achieved.

Also, for the purpose of this Focus Review, we will consider only LDPs in which the “B” is stoichiometrically substituted for two metals in different oxidation states, in other words, those that arise from heterovalent substitutions. Conversely, homovalent substitution or doping will not be covered. In the following sections, we will discuss the structure, synthesis, and general properties of the two known families of LDPs.

$\langle 100 \rangle$ -Oriented LDPs. The dimensional reduction of double perovskites can be achieved by the introduction of a large, usually organic, A-site cation. The first $\langle 100 \rangle$ -oriented halide LDPs reported were $(\text{OcDA})_2\text{Au}^{\text{I}}\text{Au}^{\text{III}}\text{I}_6\cdot\text{I}_3$ and $(\text{HpDA})_2\text{Au}^{\text{I}}\text{Au}^{\text{III}}\text{I}_6\cdot\text{I}_3$ (OcDA = octane-1,8-diammonium and HpDA = heptane-1,7-diammonium), in which the two “different” metals replacing the B site metal are Au^{I} and Au^{III} .³⁶ Interestingly, the full-inorganic 3D parent mixed-valent gold perovskites have been known since 1922.³⁷ Both the 3D and 2D versions show very distinctive AuI_6 pseudo-octahedra, indicative of the well-differentiated Au^{I} and Au^{III} ions. Then, the first mixed-metal $\langle 100 \rangle$ -oriented LDPs were reported by Karunadasa in 2018, $(\text{BA})_4\text{AgBiBr}_8$ and $(\text{BA})_2\text{CsAgBiBr}_7$ (BA = butylammonium, Figure 3A,B).³⁸ These two materials are

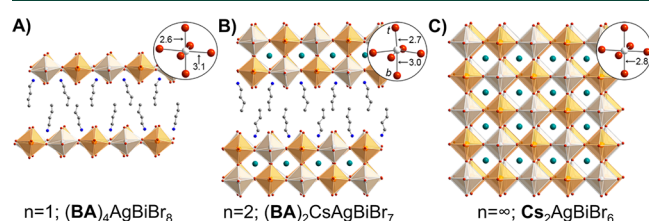


Figure 3. Single-crystal X-ray structures (298 K) of the $\langle 100 \rangle$ layered double perovskites, (A) $(\text{BA})_4\text{AgBiBr}_8$ (BA = $\text{CH}_3(\text{CH}_2)_3\text{NH}_3^+$) and (B) $(\text{BA})_2\text{CsAgBiBr}_7$, and the 3D double perovskite $\text{Cs}_2\text{AgBiBr}_6$ (C). Insets show the Ag coordination sphere with select bond distances in angstroms. In the inset for panel B, t denotes a terminal bromide and b denotes a bridging bromide. Orange, white, turquoise, brown, blue, and gray spheres represent Bi, Ag, Cs, Br, N, and C atoms, respectively. H and disordered atoms omitted for clarity.³⁸ Adapted from ref 38. Copyright 2018 American Chemistry Society.

the $n = 1$ and $n = 2$ -dimensional reductions of the 3D double perovskite $\text{Cs}_2\text{AgBiBr}_6$ (Figure 3C),³⁹ which has been extensively studied and successfully implemented as a solar cell absorber.^{40–42} These materials triggered the interest of the scientific community, leading to significant efforts to design and synthesize new LDPs. To date, hybrid LDPs have focused on the group 11 elements (Cu^{I} , Ag^{I} , and Au^{I}) together with group 13 or 15 trivalent cations: Bi, Sb, In, and Tl (Table S1 compiles all the reported LDPs). Silver(I), the most used

monovalent B^{I} cation for $\langle 100 \rangle$ -oriented LDPs, has been combined with Bi,^{38,43–53} Tl,⁵⁴ In,^{45,46} and Sb⁴⁵ to form LDPs. Although silver(I) has a d^{10} configuration without a Jahn–Teller effect, the AgX_6 octahedra present an axial contraction due to the silver(I) preference for a stable linear coordination.⁵⁵ In contrast, the $B^{\text{III}}\text{X}_6$ octahedra (Bi, Tl, and In) are considerably more regular and do not present significant distortions.

In contrast to lead halide or oxide perovskites, where purely inorganic layered structures can be obtained,^{56–58} all known $\langle 100 \rangle$ -oriented LDPs are hybrid in nature, meaning they use at least one organic A or A' cation. Also, most of these structures are single-layered ($n = 1$) and none have n values greater than 2. In fact, there are only five structures with $n = 2$: $(\text{BA})_2\text{CsAgBiBr}_7$,³⁸ $(\text{iPA})_2\text{CsAgBiBr}_7$,⁵⁰ $(\text{BA})_2\text{CsAgTlBr}_7$,⁵⁴ $(\text{PEA})_2\text{CsAgTlBr}_7$,⁵⁴ and $(\text{PA})_2\text{CsAgBiBr}_7$,⁴⁶ all of which use Cs as the small “A” cation. Future research will determine if it is possible to use other small cations such as methylammonium (MA) or formamidinium (FA) and whether it is possible to modulate the thickness of the inorganic layer past $n = 2$. Also important to note is that the reduced dimensionality of LDPs allows for further distortion of the BX_6 octahedra. Subsequently, the additional flexibility that LDPs offer allows obtaining perovskites made of combinations of metals that do not form 3D perovskites. A clear example is the formation of $(\text{PA})_4\text{AgInBr}_8$ and $(\text{PA})_2\text{CsAgInBr}_8$ perovskites (PA = propylammonium),⁴⁶ whose 3D counterpart, $\text{Cs}_2\text{AgInBr}_6$, has not been isolated yet, probably because of size mismatch between the In and the Ag octahedra.⁵⁹

The additional flexibility that LDPs offer allows obtaining perovskites made of combinations of metals that do not form 3D perovskites.

Quasi-1D LDPs. Some attempts to synthesize LDPs have resulted in materials with significant octahedral distortion that disrupts the 2D inorganic layer and thus generates quasi-1D LDPs. For instance, the incorporation of histammonium (HIS) in the LDP $(\text{HIS})_2\text{AgTlBr}_8$ results in a quasi-1D LDP, where the Ag^{I} and Tl^{III} cations have five standard metal bromide bonds and one abnormally long metal–bromide contact. The connectivity of the pentacoordinated structures favors the formation of a series of 1D chains that lay in a 2D plane. All the longer metal–bromide contacts point at the same direction and are 1.25 and 1.35 fold longer than the bonds in the same plane, with Tl–Br and Ag–Br being 2.677(1) Å and 2.777(1) Å, respectively (Figure 4A).⁵⁴ Similarly, there have been some attempts to incorporate copper(I) into LDPs.^{52,60} However, to date, they all have fallen into the quasi-1D LDP classification (Figure 4B,C). This is not particularly surprising given that Cu^{I} is notably averse to octahedral environments, which is also consistent with previous attempts to obtain Cu^{I} double perovskites that have led to non-perovskite phases containing $[\text{CuX}_4]$ tetrahedra instead.⁶¹ Indeed, all of the reported Cu^{I} quasi-1D LDP show four short bonds and two extremely long $\text{Cu}\cdots\text{I}$ interactions. In fact, these distances are close to or longer than the sum of van der Waals radii, suggesting a very weak or even a lack of interaction between them. For example, $(1,4\text{-CyDA})_2\text{CuBiI}_8\cdot 0.5 \text{H}_2\text{O}$ perovskite (1,4-CyDA = cyclohexane-1,4-diammonium)⁶⁰ shows $\text{Cu}\cdots\text{I}$ contacts of 4.03 and

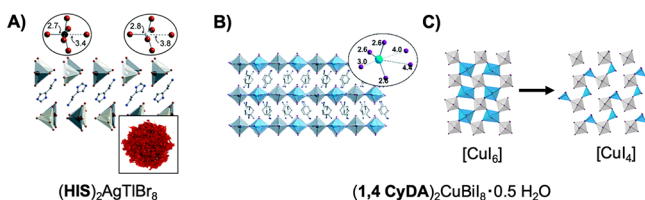


Figure 4. (A) Quasi-1D perovskite $(\text{HIS})_2\text{AgTlBr}_8$. The top inset shows the metal coordination spheres with selected bond distances in angstroms (black atom, Tl; white atom, Ag; and red atoms, Br). The bottom inset shows the color of the crystals.⁵⁴ (B) $(1,4\text{-CyDA})_2\text{CuBiI}_8 \cdot 0.5 \text{H}_2\text{O}$ perovskite. The inset shows the cooper coordination sphere with bond distances in angstroms. (C) Inorganic layer of $(1,4\text{-CyDA})_2\text{CuBiI}_8 \cdot 0.5 \text{H}_2\text{O}$ with highly distorted $[\text{CuI}_6]$ octahedra proposed by Zheng and the less strained fit with $[\text{CuI}_4]$ tetrahedra proposed in this Focus Review.⁶⁰ Adapted from (A) ref 54 and (B) ref 60 with permission of the Royal Society of Chemistry.

4.37 Å, which are almost equal or bigger than the sum of the van der Waals radii (4.1 Å).⁶²

Recently, there have also been reports of nitrate-based LDPs with the general formula: $\text{A}_4\text{B}^{\text{I}}\text{Ln}^{\text{III}}(\text{NO}_3)_8$, where A is an organic cation; B^{I} is an alkaline metal (Rb or K); and Ln^{III} represent lanthanides such as Eu, Sm, La, Dy or Ce.^{63,64} As will be discussed later, these nitrate-LDPs have interesting ferroelectric and luminescent properties. Further, these Ln-structures suggest that it should also be possible to incorporate lanthanides in the B^{III} site and different inorganic anions in the halide site into LDPs, which could in turn result in exciting optical properties.

Synthesis of $\langle 100 \rangle$ -LDPs. By far the most common method of synthesis for $\langle 100 \rangle$ -oriented LDPs is the liquid-phase crystallization, which involves dissolving stoichiometric amounts of the metal halides or oxides and the amine/ammonium in halohydric acidic medium. Another synthetic route is the solid-state reaction with a mixture of the metal and ammonium halides at $\sim 150^\circ\text{C}$.⁴⁵ Both methodologies have been successful at obtaining $\langle 100 \rangle$ -oriented LDPs. Structural characterization of these materials has been achieved primarily by single-crystal X-ray diffraction (SCXRD), which allows for unequivocal identification of the crystal structure, including the inorganic layer thickness (n -value). Complementary, powder X-ray diffraction (PXRD) is useful to corroborate bulk-purity, preferential orientation on a substrate, and sometimes the n -value. However, PXRD is ineffective for complete structural elucidation, as the presence of poorly diffracting organic cations embedded in highly diffracting inorganic layers is not amenable to *de novo* methods. Importantly, most of these materials are remarkably stable, with some showing decomposition temperatures past 300°C and most being able to tolerate water, humidity, and oxygen rather well.⁴³

Unlike 3D perovskites and double perovskites (DPs), the number of possible organic cations incorporated in hybrid LDPs is enormous. Indeed, many organic cations have already been incorporated in hybrid LDPs (see Figure 5). The importance of the organic cations in perovskites has been extensively demonstrated in lead and tin perovskites, and the results can be extrapolated to the emerging layered double perovskites. For instance, organic cations have been used to modulate some properties like the octahedron distortion,⁶⁵ the

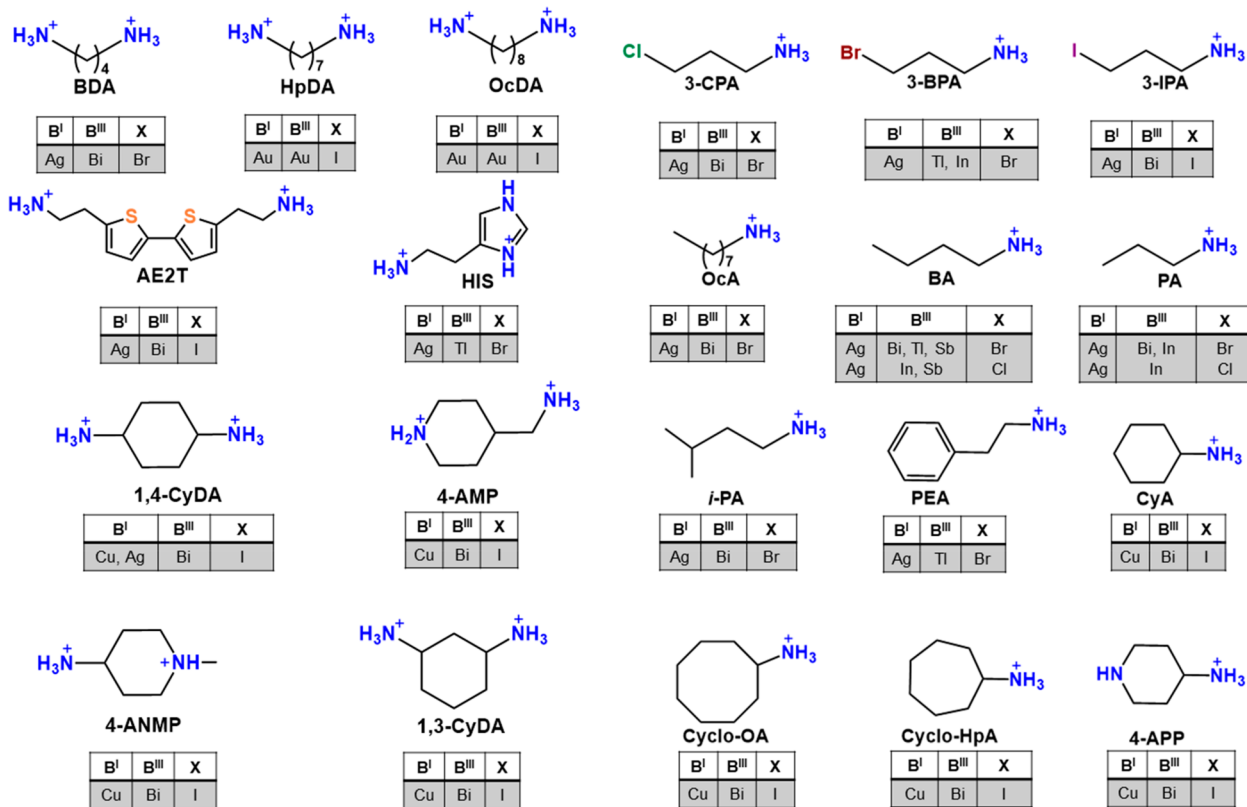


Figure 5. Cations and anions used in hybrid organic–inorganic LDPs. The tables under the molecules summarize which B^{I} inorganic monovalent cation, B^{III} inorganic trivalent cation, and X halogen have been used with each organic cation. The reference for each material can be found in Table S1.

perovskite phase (Dion–Jacobson DJ or Ruddlesden–Popper RP),⁶⁶ the chiroptical properties,^{67,68} and the photoluminescence,⁶⁹ among others. In hybrid LDPs some of these strategies are already being employed. For example, when an organic dication is used, the DJ phase is preferred, while a monovalent cation forms a RP phase.⁴⁶ Supramolecular interactions have also been harnessed in LDPs. For example Mitzi and co-workers proposed that the supramolecular face–edge aromatic interaction of the cation 5,5'-diylbis-(aminoethyl)-[2,2'-bithiophene] (AE2T) stabilizes the iodide perovskite [(AE2T)₂AgBiI₈]. In contrast, the absence of important supramolecular interactions in the BA cation does not favor the formation of the layered iodide perovskite BA₄AgBiI₈, but rather the formation of 0D and 1D materials.⁴³ Similarly, the importance of supramolecular interactions has also been highlighted in the synthesis of (3-BPA)₄AgTlBr₈ (3-BPA = 3-bromopropylammonium), which shows a significantly decreased disorder compared to the BA and PEA (phenethylammonium) cations. This observation suggests that the weak C–Br⋯Br–M interaction has an important role directing the crystallization.⁵⁴

Within the ⟨100⟩-LDPs, two subcategories can be found: RP and DJ perovskites depending on the alignment or lack thereof between the inorganic layers (Figure 6). In the DJ phases, the

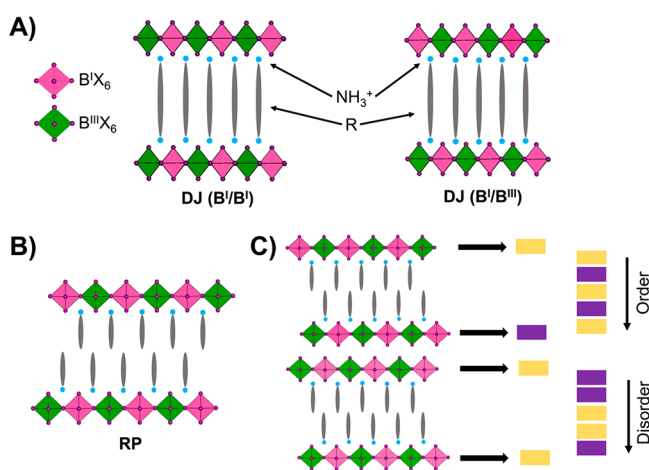


Figure 6. B^IX₆ and B^{III}X₆ are represented by pink and green octahedra, respectively. (A) Schematic representation of DJ phase. Left: DJ phase with top-to-top stacking B^I/B^I. Right: DJ phase with B^I/B^{III} stacking. (B) RP phase and (C) stacking of inorganic layers and order or random stacking in double perovskites.

layers lie on top of each other (Figure 6A), whereas in the RP phases, the layers are shifted between each other (Figure 6B). Furthermore, the two B^IX₆ and B^{III}X₆ octahedra increase the number of stacking possibilities between the layers, which results in two DJ phases, DJ (B^I/B^I) and DJ (B^I/B^{III}), portrayed in Figure 6A. Despite the increased stacking possibilities, most reported crystal structures have a reproducible order without observed stacking-fault, neither by stacking mixture of DJ-B^I/B^I and B^I/B^{III} phases nor by RP stacking fault (Figure 6C). It will be interesting to determine if this true for all LDPs and whether this has significant effects on the electronic structure of these materials.⁶³

Optoelectronic properties of ⟨100⟩-LDPs. Hybrid LDPs are the merging of layered and double perovskites, and therefore, we are prompted to ask what new optoelectronic properties will emerge, or whether the optoelectronic properties of one family

will prevail over the other. We are still at the start of this new path in the perovskite realm; hence, many questions remain unanswered and some discrepancies can be found among different studies. Herein, we intend to give a general landscape and trends of the optoelectronic properties of ⟨100⟩- and ⟨111⟩-LDPs.

In the conventional 3D lead halide perovskite APbX₃, the valence band maximum (VBM) is made of hybridized Pb 6s/I 5p states and the conduction band minimum (CBM) of Pb 6p states. Many studies have shown that the lone 6s² pair plays a critical role in the superior optoelectronic properties of lead halides perovskites.⁷⁰ Thus, to find suitable replacements for Pb, one would like to retain a similar electronic structure. In this context, X. Zhao⁷¹ and co-workers proposed a classification for double perovskites based on the lone-pair *ns* states of the B^I and B^{III} cations. The classification is as follows: when both cations have filled *ns*² lone pairs, they classify as type I; if B^I has empty *s*⁰ states, they are type II; when both cations have empty *s*⁰ states, they are type III. This classification is also useful for LDPs and will be used for this Focus Review.

Hybrid LDPs are the merging of layered and double perovskites; therefore, we are prompted to ask what new optoelectronic properties will emerge, or whether the optoelectronic properties of one family will prevail over the other.

⟨100⟩-LDPs reported so far are either type II or III, and among type II, most incorporate Ag^I and Bi^{III} with different organic ligands. In general, type II LDPs have a similar electronic structure to 3D double perovskites. The VBM is derived from hybridized B^I d/halogen p states with some contribution from B^{III} s states, while the CBM is derived from hybridized B^{III} p/halogen p orbitals with some contribution from B^I s states. The orbital overlap with neighboring octahedra to produce dispersive electronic states is defined as electronic dimensionality.⁷³ The Ag^I/Bi^{III}3D structure has low electronic dimensionality because the frontier orbitals are confined to either silver or bismuth, which leads to a more localized, narrow conduction band, and a large bandgap.⁷² Because the electronic structure of Ag^I/Bi^{III} LDPs is very similar to their 3D counterpart, it is only natural that these perovskites also have low electronic dimensionality. Furthermore, upon reduction of structural dimensionality, the electronic properties become highly anisotropic and band dispersion also produces flat bands.⁷⁴ Overall, for Ag^I/Bi^{III} LDPs both electronic and dimensional reduction affect the electronic properties producing low dispersion of the bands and typically leading to either isoenergetic or small-difference direct and indirect bandgaps.

In the 3D structure Cs₂AgBiX₆,⁷⁵ the presence of Ag 4d states plays a role in reducing the bandgap and is partially responsible for the indirect bandgap of the material. This can also be tuned by changing the B^I/B^{III} combinations⁷⁶ or by introducing disorder in the octahedra.⁷⁷ For LDPs, this can also be achieved through dimensional reduction. The effects of dimensional reduction on the electronic structure were studied with DFT calculations by several groups. For example, the materials with *n* ≥ 2 in the (BA)₄AgBiBr₈ system have

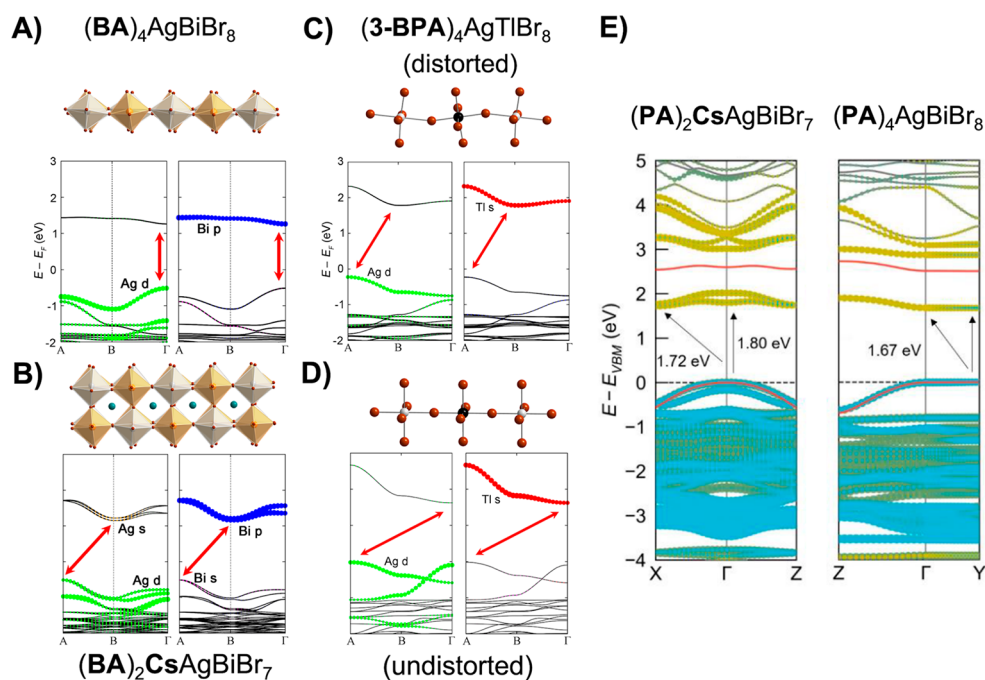


Figure 7. (A) $(\text{BA})_4\text{AgBiBr}_8$ ($n = 1$) and (B) $(\text{BA})_2\text{CsAgBiBr}_7$ ($n = 2$), dimensional reduction from $n = 2$ to $n = 1$ produces a transition from indirect to direct bandgap. Figure adapted from ref 38. Band structure of the (C) distorted and (D) undistorted $(3\text{-BPA})_4\text{AgTlBr}_8$.⁵⁴ Adapted from ref 54 with permission of The Royal Society of Chemistry. (E) Dimensional reduction of $(\text{PA})_2\text{CsAgBiBr}_7$ to $(\text{PA})_2\text{AgBiBr}_8$. Both materials maintain almost equal direct and indirect bandgaps.⁴⁶ Adapted from ref 46. Copyright 2020 American Chemical Society.

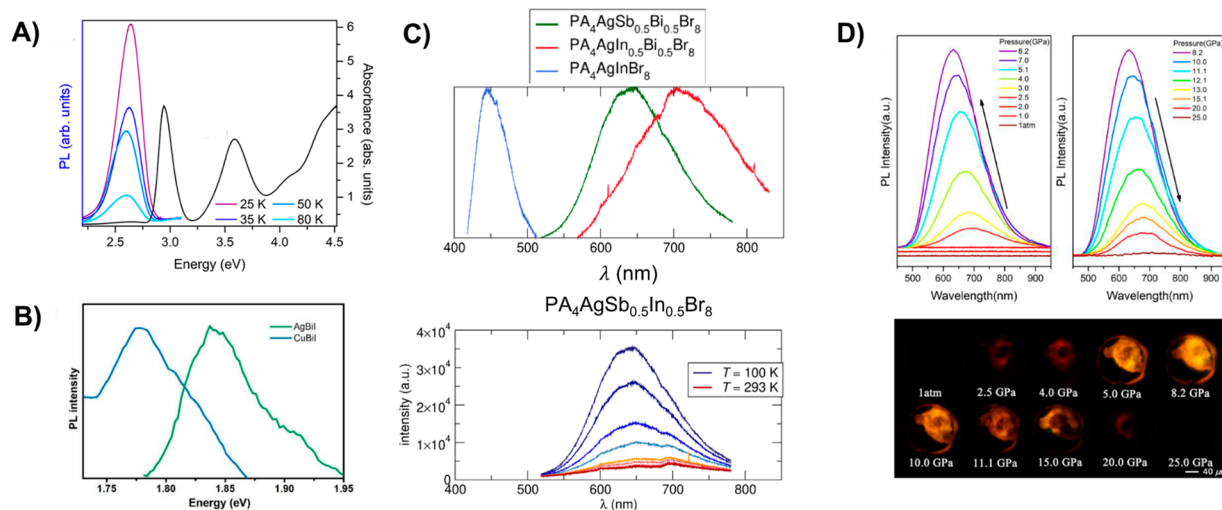


Figure 8. (A) Low-temperature quenching broadened PL emission from $(\text{BA})_4\text{AgBiBr}_8$ (colored lines).³⁸ Copyright 2018 American Chemical Society. (B) PL emission from $(1,4\text{-CyDA})_2\text{AgBiBr}_8 \cdot \text{H}_2\text{O}$ and $(1,4\text{-CyDA})_2\text{CuBiBr}_8 \cdot 0.5\text{H}_2\text{O}$.⁵² Adapted from ref 52 with permission of The Royal Society of Chemistry. (C) Top: broad white emission from $(\text{PA})_4\text{AgIn}_{0.5}\text{Bi}_{0.5}\text{Br}_8$ and $(\text{PA})_4\text{AgSb}_{0.5}\text{Bi}_{0.5}\text{Br}_8$ LDPs, probably originating from STES. Bottom: temperature PL quenching of $(\text{PA})_4\text{AgSb}_{0.5}\text{Bi}_{0.5}\text{Br}_8$.⁴⁶ Copyright 2020 American Chemical Society. (D) PL emission at different pressures of $(\text{BA})_4\text{AgBiBr}_8$.⁴⁴ 2020 Wiley-VCH Verlag GmbH & Co. KGaA, Weinheim.

analogous electronic structures with indirect bandgaps and decreasing band dispersion for lower values of n .³⁸ When the thickness of the layer decreases to $n = 1$, the electronic structure suffers a transition from indirect to direct bandgap as the VBM becomes mainly composed of Ag s/Br p states and the CBM of Bi p/Br p states (Figure 7A,B). Although dimensional reduction accounts for the indirect-to-direct bandgap transition, band dispersion was further increased by the organic cation structural-induced distortions (Figure 7C,D). This effect is similar in hybrid lead halide perovskites where the organic cation orbitals do not usually contribute to

the band edges, but its interaction with the halides of the inorganic layer can influence the magnitude and the nature of the bandgap.^{25,73} Furthermore, dimensional reduction proved having little effect on the localized Bi p states that generate the near-band edge optical transitions in the $(\text{BA})_4\text{AgBiBr}_8$ absorbance spectra, which translates in the $n = 1$ and $n = 2$ materials having very similar yellow colorations (Figure 8A). On the other hand, Seshadri studied dimensional reduction on the same Ag/Bi system with the PA^+ organic spacer and found that indirect and direct bandgaps are isoenergetic, but this time, a slight bandgap decrease is observed when the number

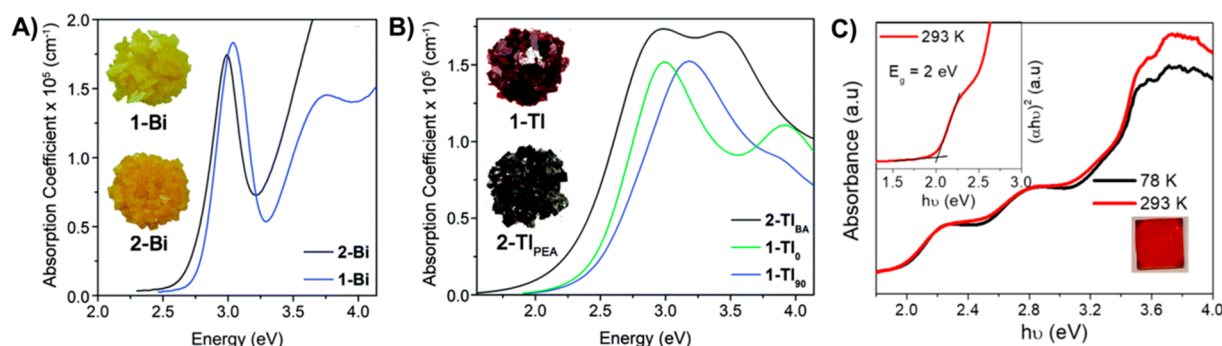


Figure 9. Absorption spectra show broadened absorption bands near the absorption band edge. For (A) $(\text{BA})_4\text{AgBiBr}_8$ (1-Bi) and $(\text{BA})_2\text{CsAgBiBr}_7$ (2-Bi), (B) $(3\text{-BPA})_4\text{AgTlBr}_8$ (1-Tl) and $(\text{PEA})_2\text{CsAgTlBr}_7$ (2-Tl_{PEA}),⁵⁴ the band-edge absorption bands correspond to an almost pure metal B^{I} to metal B^{III} charge transfer band. For (C) $[\text{AE2T}]_2\text{AgBiI}_8$, the transition involves $\text{I}_{\text{eq}} \text{p}$ states in the VBM and hybridized Bi p and $\text{I}_{\text{eq}} \text{p}$ in the CBM.⁴³ (A and B) Adapted from ref 54 with permission of The Royal Society of Chemistry. (C) Adapted from ref 43. Copyright 2020 American Chemical Society.

of layers decreases to $n = 1$ (Figure 7E). They proposed that the organic spacer and the choice of functional can change the location of the CBM while band dispersion remains unchanged and that the type of structure (RP/DJ) could be of greater importance than the layering in the Ag/Bi/Br system. They also hypothesize that the organic spacer has a minimal effect on the magnitude of the bandgap, as $(\text{BDA})_2\text{AgBiBr}_8$ and $(\text{Oca})_4\text{AgBiBr}_8$ have very similar bandgaps compared to $(\text{PA})_4\text{AgBiBr}_8$ (2.43, 2.45, and 2.41 eV, respectively).⁴⁶ Importantly, most $n = 1$ Ag/Bi LDPs have direct bandgaps but a few report indirect ones, such as $(3\text{-CPA})_4\text{AgBiBr}_8$ and $(1,4\text{-CyDA})_2\text{AgBiBr}_8$.^{49,52} The origin of the seeming lack of trend regarding the nature of the bandgap for Ag/Bi LDPs and the band dispersion is still unknown; further studies will determine if the organic cations play a larger part in the electronic structure of these new layered perovskites.

The magnitude of the bandgap follows the expected trend; the energy of the halogen p states increases when moving down in the periodic table, increasing the overlap between the larger orbitals of the iodide sublattice as both bands are derived from the halogen p states. This in turn decreases the magnitude of the bandgap, with values around ~ 2.5 eV for bromides and ~ 2.0 eV for iodides. Further, McClure found that the bandgap of Ag/Bi LDPs is smaller than the bandgap of the Ag/Sb LDPs, which contradicts the general trend.⁴⁵ This anomalous behavior has been ascribed to the relativistic contraction of the Bi 6s orbital that results in a more localized, lower-energy valence s orbital, compared to the Sb 5s lone pair.⁷⁸

In most $\langle 100 \rangle$ -LDPs and akin to 3D DP, the PL emission either quenches upon warming or has low intensity at room temperature (Figure 8A–D). This dramatically differs from group 14 halide perovskites, where strong sharp excitonic and luminescence features are stabilized at room temperature as a consequence of dimensional reduction.⁶⁹ It has been hypothesized that the origin of the weak PL emission in $\langle 100 \rangle$ -LDPs originates from a defect-mediated PL mechanism³⁸ or from the localization of the photogenerated holes on the Ag-containing octahedra with the Bi-containing octahedra unable to undergo radiative recombination.⁴³

It is well-known that doping and elemental substitution can alter the properties of double-perovskite compounds.^{79–81} For example, $(\text{PA})_4\text{AgIn}_{0.5}\text{Bi}_{0.5}\text{Br}_8$ and $\text{PA}_4\text{AgSb}_{0.5}\text{Bi}_{0.5}\text{Br}_8$ LDPs alloys (Figure 8C) exhibit broad low-intensity luminescence with large Stokes shifts that probably originate from self-

trapped excitons (STEs) arising from electron–phonon coupling. Importantly, the pure $(\text{PA})_4\text{AgInBiBr}_8$ presents a much narrower emission (with a full width at half-maximum fwhm of 50 nm) and the emission of $(\text{PA})_4\text{AgBiBr}_8$ or $(\text{PA})_4\text{AgSbBr}_8$ is too weak to be observable at room temperature.⁴⁶ This type of behavior is quite similar to extrinsic self-trapping in Sn-doped $(\text{PEA})_2\text{PbI}_4$ layered perovskites where the emerging broadband emission arises from the interplay of impurity-driven exciton accumulation and the strong exciton–phonon coupling.⁸² Intrinsic self-trapping does not require lattice defects, and together with extrinsic self-trapping emission, both contribute to white emission in lead halide perovskites.⁶⁹ In this context, LDPs could be a great platform for STE emission because low dimensionality and localized electrons and holes are known to facilitate octahedral distortion and STE formation in halide perovskites.⁸³ Further, very high PLQYs have been obtained for the DP $\text{Cs}_2\text{Na}_x\text{Ag}_{1-x}\text{InCl}_6$, where STE emission was stabilized and enhanced by disrupting the parity-forbidden transitions in the crystal structure⁸⁴ and by increasing the overlap between the wave function distributions of electrons and holes with Na^+ doping. In addition, Bi^{3+} doping also helped to suppress nonradiative defects.⁸⁵ In LDPs, broad photoluminescence has been achieved in $(\text{BA})_4\text{AgBiBr}_8$ by applying pressure, which resulted in stronger phonon coupling and stable STEs (Figure 8D).⁴⁴ The stronger emission was paired with a bandgap narrowing due to a reconfiguration of the VBM and CBM orbitals.

In the absorption spectra of most Ag/Bi LDPs, broad features near the band edge absorption have been observed. Although it is tempting to interpret them as excitonic broadened absorption bands, as in layered halide Pb perovskites, the weak temperature dependence and the absence of band-edge PL do not support an excitonic transition. Instead, the transitions associated with these features have different origins: in $(\text{BA})_4\text{AgBiBr}_8$, the transition is attributed to an almost pure Ag-to-Bi metal-to-metal charge transfer (MMCT), whereas in $(\text{AE2T})_2\text{AgBiI}_8$, the transitions occur between equatorial $\text{I}_{\text{eq}} \text{p}$ states in the VBM and hybridized Bi p and $\text{I}_{\text{eq}} \text{p}$ states in the CBM, leaving little room to be an almost pure MMCT transition (Figure 9 A–C). In both cases, the transitions differ from Pb halide perovskites, where charge transfer (CT) transitions occur within VBM Pb p to CBM Pb p states.

Type III LDPs have spherically symmetric ns Tl^{III} or In^{III} orbitals that contribute significantly to the CBM and Ag d/X p orbitals that contribute to the VBM. Unlike the directional Bi p states, the symmetric s orbitals promote electronic delocalization of the electron wave functions in the CBM, which increases the effects of dimensional reduction.⁴⁷ For example, in Ag/Tl/Br LDPs, the optical spectrum drastically changes with decreasing n as evidenced by the change in color from black for $n = 2$ ($\text{PEA}_2\text{CsAgTlBr}_7$) to red for $n = 1$ ($3\text{-BPA}_4\text{AgTlBr}_8$) (Figure 9B). Furthermore, the band near the absorption edge in the absorption spectra ascribed to Ag/Tl MMCT broadens, the band dispersion decreases, and the bandgap increases. A transition from direct to indirect bandgap occurs as the VBM becomes almost entirely composed of Ag d and Br p orbitals and CBM from Tl s and Br p orbitals.

The In-containing compounds have larger bandgaps than the Tl materials because of the higher energy of the conduction band. However, similarly to the Tl materials, $(3\text{-BPA})_4\text{AgInBr}_8$ also shows a direct-to-indirect transition upon dimensional reduction.⁴² Interestingly, the transition from direct-to-indirect in type III LDPs upon dimensional reduction is exactly the inverse as in type II LDPs, which raises the question of whether it is a general trend.⁴⁷ When Ag^{I} is replaced with Cu^{I} , the higher-lying Cu 3d states hybridize with Cl 3p states, reducing the bandgap. This was observed in several Cu/In LDPs, such as $(\text{BA})_4\text{AgInCl}_8$ and $(\text{BA})_4\text{CuInCl}_8$ with 4.27 and 3.47 eV bandgaps, respectively.⁴⁵ A similar trend is observed $(1,4\text{CyDA})_2\text{AgBiI}_8 \cdot \text{H}_2\text{O}$ ($E_g = 1.93$ eV) and $(1,4\text{CyDA})_2\text{CuBiI}_8 \cdot 0.5\text{H}_2\text{O}$ ($E_g = 1.68$ eV).⁵²

<111>-Oriented LDPs. Unlike all the other layered perovskites, in $\langle 111 \rangle$ -oriented layered perovskites, the layering is

Unlike all the other layered perovskites, in $\langle 111 \rangle$ -oriented layered perovskites, the layering is generated by the introduction of vacancies and not from the incorporation of large organic cations.

generated by the introduction of vacancies and not from the incorporation of large organic cations. The single-metal, lower- n members ($n = 2$) of this family of perovskites are relatively well-known, and the first reports date back to the 1930s.⁸⁶ Moreover, some of these materials, such as $\text{Cs}_3\text{Sb}_2\text{I}_9$ and $\text{Cs}_3\text{Bi}_2\text{Cl}_9$, have been successfully implemented in solar cells⁸⁷ and X-ray photodetectors.⁸⁸ Nevertheless, it was not until 2017 that our group reported the first $\langle 111 \rangle$ -oriented LDP (and the first mixed-metal LDP), $\text{Cs}_4\text{CuSb}_2\text{Cl}_{12}$.³⁴ This material can be visualized as the extended structure of $\langle 111 \rangle$ -oriented perovskites with formula $\text{A}_3\text{B}_2^{\text{III}}\text{X}_6$, in which an additional layer of CuCl_6 octahedron has been inserted between the SbCl_6 octahedron layers to form a three-octahedra thick inorganic slab (Figure 10B,C). The $\langle 111 \rangle$ -oriented LDPs, also referred as “quadruple perovskites,” can be derived from 3D double perovskites ($\text{A}_2\text{B}^{\text{I}}\text{B}^{\text{III}}\text{X}_6$) where B^{I} is replaced by B^{II} and a vacancy (\square) (Figure 10A) and have the general formula $\text{A}_4\square\text{B}^{\text{II}}\text{B}_2^{\text{III}}\text{X}_{12}$. $\text{Cs}_4\text{CuSb}_2\text{Cl}_{12}$ has a small bandgap of 1.0 eV, which is particularly surprising when considering that its “parent” structure, the single-metal perovskite $\alpha\text{-Cs}_3\text{Sb}_2\text{Cl}_9$, has a bandgap of 3.0 eV. Besides its attractive bandgap, suitable for photovoltaic applications, $\text{Cs}_4\text{CuSb}_2\text{Cl}_{12}$ showed remarkable

stability and easy synthesis, which allows synthesis in the gram-scale by several methods and in different forms, such as single-crystals;^{34,89} microcrystalline powders;^{34,90} films;^{91,92} and more recently, nanocrystal NCs.^{91,92}

The discovery of $\text{Cs}_4\text{CuSb}_2\text{Cl}_{12}$ motivated the search for more $\langle 111 \rangle$ -oriented LDPs by different groups and different approaches. Generally, the methodology to predict stable $\langle 111 \rangle$ -oriented LDPs consists of two steps: first, an empirical extended Goldschmidt parameter specific to this kind of material; and second, DFT calculations to evaluate their stability relative to known decomposition products.^{93,94} The latter defines the thermodynamic stability of the materials,⁹⁵ while the former defines the limit of the perovskite structural stability by empirical statistics of the effective tolerance factor t_{eff} and the effective octahedral factor μ_{eff} [$0.81 < t < 1.11$ and $0.41 < \mu < 0.90$]. The extended Goldschmidt parameters (t_{eff} and μ_{eff}) take into account both cations in the $\text{A}_4\text{B}^{\text{II}}\text{B}^{\text{III}}\text{X}_{12}$ perovskites as follows (eqs 1 and 2):⁹⁴

$$\text{A}_4\text{B}^{\text{II}}\text{B}^{\text{III}}\text{X}_{12}: t_{\text{eff}} = \frac{R_{\text{A}} + R_{\text{X}}}{\sqrt{2 \left\{ \frac{(R_{\text{B}^{\text{II}}} + R_{\text{B}^{\text{III}}})}{3} + R_{\text{X}} \right\}}} \quad (1)$$

$$\mu_{\text{eff}} = (R_{\text{B}^{\text{II}}} + 2R_{\text{B}^{\text{III}}})/3R_{\text{X}} \quad (2)$$

where R_{A} , $R_{\text{B}^{\text{II}}}$, $R_{\text{B}^{\text{III}}}$, and R_{X} represent the Shannon ionic radii of the A, B^{II} , B^{III} , and X ions, respectively.

This methodology has been successfully employed to accelerate the discovery of $\langle 111 \rangle$ -LDPs which has resulted in the discovery of several new materials.^{93,94} The addition of these new materials has significantly expanded the chemical space of $\langle 111 \rangle$ -LDPs, so that to date, Cu, Mn, and Cd have been placed in the B^{II} site and Sb and Bi the B^{III} position (Figure 11). While these metals and their permutations allow for a significant amount of materials, there are also calculations that predict the stability of perovskites with other B^{II} cations, namely, Zn, Fe, Cr, Sn, Ca, Mg, Sr, and Sc.^{93,94,96} On the other hand, the theoretical and experimental results have been limited to Bi and Sb as B^{III} cation. This is an important area of opportunity, as there are no intrinsic reasons to discard other trivalent metals, such as Fe or As that are known to form $\langle 111 \rangle$ -oriented perovskites.^{86,97} Other elements like Tl and In could also be taken into account because they can form $\langle 100 \rangle$ -LDPs and 3D double perovskites.^{54,71} Yet another avenue is the incorporation of lanthanides (Ln^{III}) known to form elpasolite structures and are suitable dopants in other halide perovskite phases.⁹⁸ Importantly, the exploration of this family of materials could be accelerated because they are amenable to high-throughput computational methods, automated synthesis, or machine learning characterization and diagnosis.⁹⁹

From the halide perspective, it is worth noting that, to date, all of the experimentally isolated $\langle 111 \rangle$ -LDPs use chloride as the halide.^{34,93,100–102} According to the extended Goldschmidt predictions, this can be solved by the insertion of large B^{III} cations, such as Bi or lanthanide ions that could allow the formation of bromide or iodide $\langle 111 \rangle$ -LDPs. The incorporation of other halides would be of particular interest because of the halogen contribution to the band edges, and therefore, the possibility to tune the bandgap, similarly to what has been done for other halide perovskites.¹⁰³ Yet another avenue of research is to explore other A- and A'-site cations, because currently, only Rb and Cs have been successfully employed in the synthesis of $\langle 111 \rangle$ -LDPs (Figure 11). While some of our early attempts to introduce organic cations, such as MA or FA

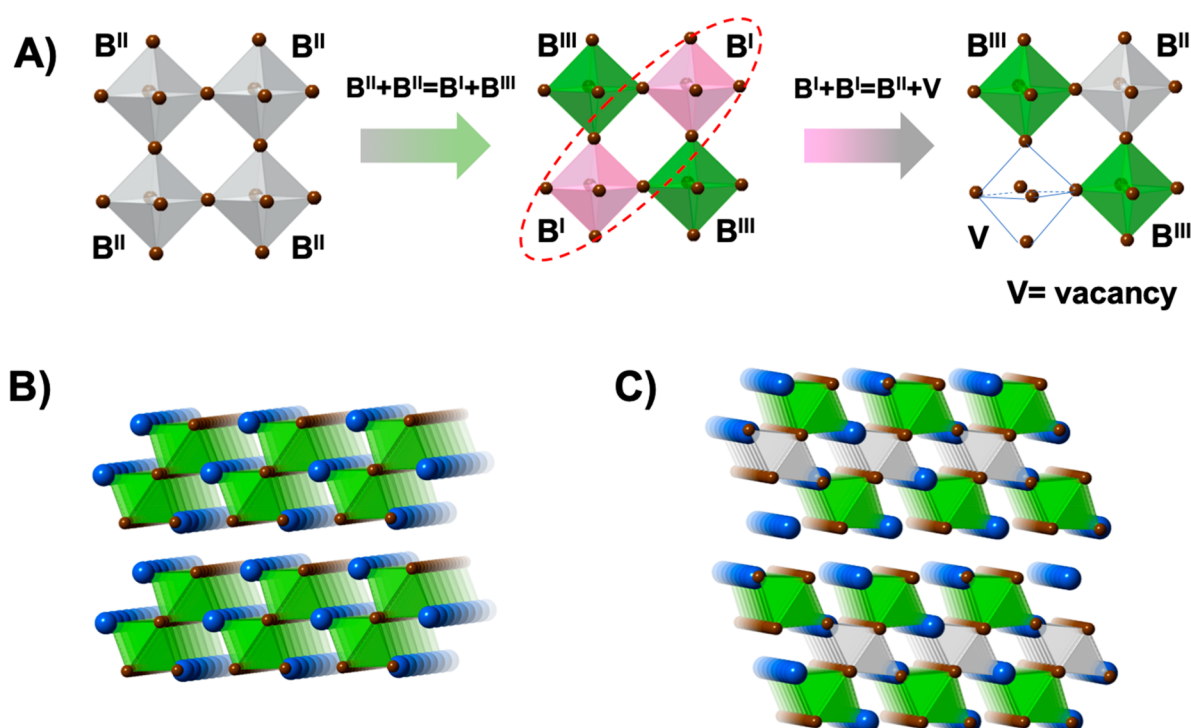


Figure 10. (A) Schematic illustration of the B cation transmutation. (B and C) Crystal structures of α - $\text{Cs}_3\text{Sb}_2\text{Cl}_9$ and $\text{Cs}_4\text{CuSb}_2\text{Cl}_{12}$, respectively. Cl and Cs atoms are depicted as brown and blue spheres, respectively; Sb and Cu coordination polyhedra are shown in green and gray, respectively.

A				B ^{II}				B ^{III}				X			
4				2				12							
	Ca*														Cl
	Mg*	Sc*	...	Cr*	Mn	Fe*	...	Cu	Zn*		Ge*				Br*
Rb	Sr*			Cd	In*	Sn*	Sb			I*
Cs					Tl*	Pb*	Bi			

Figure 11. Periodic table of cations (A, B^{II}, and B^{III}) and anions (X⁻) that have been used in $\langle 111 \rangle$ -oriented halide LDPs. Elements marked with an asterisk (*) denote elements that have been computationally predicted to form stable $\langle 111 \rangle$ -LDPs but are still awaiting experimental confirmation.

have failed, it is still very much in play that those organic cations or even larger ones could be used for the synthesis of $\langle 111 \rangle$ -LDPs. In the meantime, one of the advantages of having fully inorganic LDPs is their thermal stability. Most decomposed well above 200 °C and sometimes even above 300 °C. Further, many of these materials have shown remarkable stability toward humidity and light.^{93,101}

Another possibility to modify or tune the electronic properties of $\langle 111 \rangle$ -LDPs is to alloy metals in the B^{II} or B^{III} position. This approach was first demonstrated by alloying Mn in $\text{Cs}_4\text{CuSb}_2\text{Cl}_{12}$ to form the family of materials with formula $\text{Cs}_4\text{Cu}_{1-x}\text{Mn}_x\text{Sb}_2\text{Cl}_{12}$, which showed full Mn-solubility and a remarkable ability to modulate the bandgap of the compounds in a range of almost 2 eV (Figure 12 A).¹⁰⁰ Later, it was also demonstrated that Mn could also be alloyed into other families of $\langle 111 \rangle$ -LDPs, $\text{Cs}_4\text{Cd}_{1-x}\text{Mn}_x\text{Sb}_2\text{Cl}_{12}$ and $\text{Cs}_4\text{Cd}_{1-x}\text{Mn}_x\text{Bi}_2\text{Cl}_{12}$, which resulted in interesting luminescent and magnetic properties (Figure 12B,C), as will be discussed

later. Similarly, the B^{III} position is also susceptible to metal alloying, as has been demonstrated in the family of materials with formula $\text{Cs}_4\text{Cd}_{0.8}\text{Mn}_{0.2}\text{Sb}_{2-y}\text{Bi}_y\text{Cl}_{12}$.¹⁰² The ability to alloy both, B^{II} or B^{III}, is exciting as it might allow fine-tuning these materials for specific applications.

Synthesis of $\langle 111 \rangle$ -LDPs. The synthesis of $\langle 111 \rangle$ -oriented LDPs has been mostly achieved by their precipitation from concentrated hydrochloric acid solution or by mechanochemical reaction. The starting materials are usually the metal halides or oxides. For example, the $\text{Cs}_4\text{CuSb}_2\text{Cl}_{12}$ perovskite was synthesized by precipitation of a solution of Sb_2O_3 , CsCl , and CuCl_2 in hydrochloric acid, with a yield of 90.8%.³⁴ The same perovskite can be obtained by mechanochemical reaction at room temperature, grinding the salts SbCl_3 , CsCl , and CuCl_2 , with almost 100% of conversion.⁹⁰ Unlike, $\langle 100 \rangle$ -oriented LDPs, $\langle 111 \rangle$ -oriented LDPs can be structurally characterized by both SCXRD and PXRD, as their inorganic nature is amenable to both techniques. PXRD can also be used to corroborate the bulk-purity and preferential orientation of $\langle 111 \rangle$ -oriented LDPs.

Another interesting approach for LDPs is the synthesis of colloidal nanoparticles (NPs). The synthesis of colloidal NPs of $\text{Cs}_4\text{CuSb}_2\text{Cl}_{12}$ was demonstrated by Chen and co-workers, who used the hot-injection method to synthesize sphere-shaped nanoparticles with an average diameter of 12.5 ± 1.9 nm.⁹¹ Similarly, Wang et al. demonstrated that it is also possible to obtain colloidal NPs of $\text{Cs}_4\text{CuSb}_2\text{Cl}_{12}$ by exfoliating larger crystallites of $\text{Cs}_4\text{CuSb}_2\text{Cl}_{12}$ using a surfactant and an ultrasonic bath.⁹² While the NCs synthesis has been employed only for $\text{Cs}_4\text{CuSb}_2\text{Cl}_{12}$ to date, this report opens the possibility to extend the synthetic methods to achieve the size and shape control of many other LDPs.

Magnetic Properties. Several efforts to investigate the electronic structure of $\langle 111 \rangle$ -oriented layered perovskites

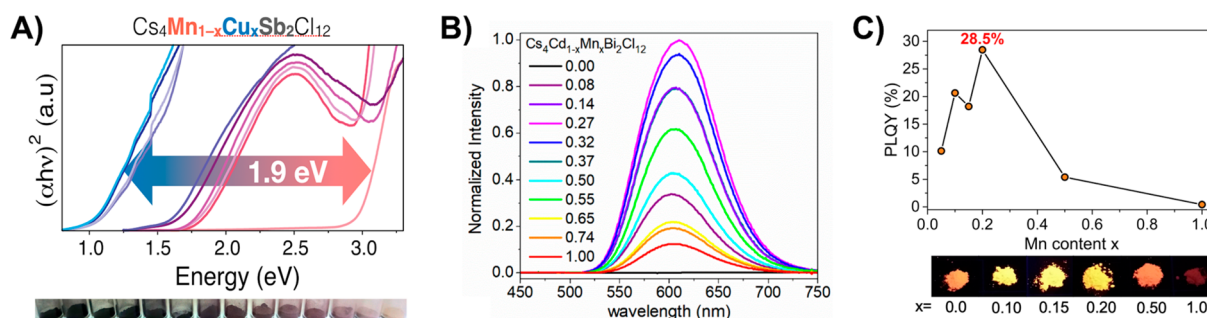


Figure 12. (A) Top: Tauc plots of $\text{Cs}_4\text{Mn}_{1-x}\text{Cu}_x\text{Sb}_2\text{Cl}_{12}$; from left (blue) to right (pink): $x = 1.0, 0.8, 0.6, 0.5, 0.3, 0.2, 0.1, 0.05, 0.01$, and 0.0 . Note that concentrations of Cu less than 5% ($x = 0.05$) are better described as dopants, and as such, Tauc plots of these materials are shown only for comparison purposes. Bottom: Picture of vials containing microcrystalline $\text{Cs}_4\text{Mn}_{1-x}\text{Cu}_x\text{Sb}_2\text{Cl}_{12}$ samples with x values of $0.0, 0.002, 0.005, 0.02, 0.03, 0.05, 0.1, 0.2, 0.3, 0.4, 0.5, 0.6, 0.8$, and 1.0 from left to right, respectively. (B) Emission spectra of $\text{Cs}_4\text{Mn}_{1-x}\text{Cd}_x\text{Bi}_2\text{Cl}_{12}$ with increasing Mn content synthesized by Woodward and reaching a maximum PLQY of 57%. (C) A 28.5% PLQY was attained for a 20% Mn content for $\text{Cs}_4\text{Mn}_{1-x}\text{Cd}_x\text{Sb}_2\text{Cl}_{12}$.¹⁰⁰ Adapted from (A) ref 100, (B) ref 105, and (C) ref 102. Copyright 2018 and 2020 American Chemical Society.

through DFT calculations have been made. It is important to notice that because of the presence of metals with unpaired electrons, such as Cu or Mn, the magnetic configurations have to be taken into account for accurate calculations. For the Mn/Cu family of materials, $\text{Cs}_4\text{Cu}_{1-x}\text{Mn}_x\text{Sb}_2\text{Cl}_{12}$, the most stable antiferromagnetic (AFM) configuration has intralayer antiferromagnetism, where each CuCl_6 octahedral chain along the [010] direction is antiferromagnetic.¹⁰⁴ The antiferromagnetic behavior of $\text{Cs}_4\text{Cu}_{1-x}\text{Mn}_x\text{Sb}_2\text{Cl}_{12}$ has also been corroborated experimentally, and similarly, the family of materials $\text{Cs}_4\text{Cd}_{1-x}\text{Mn}_x\text{Bi}_2\text{Cl}_{12}$ has also proven to have antiferromagnetic properties.^{101,105}

Optoelectronic Properties of $\langle 111 \rangle$ -LPDs. In general, the inorganic $\langle 111 \rangle$ -LDPs orbital contribution to the band edges is as follows: the VBM is composed of Cl p and B^{III} s orbitals and B^{II} d orbitals; the CBM is composed of Cl p and B^{III} p orbitals and B^{II} d states. This band orbital composition is quite different from $\langle 100 \rangle$ -LDPs. For the latter, the B^{I} contributes to the VBM with s orbitals and to the CBM with d orbitals. In inorganic LDPs, the B^{II} metals Cu^{II} , Mn^{II} , and Cd^{II} contribute to both bands with B^{II} d states. Because transitions between d–d states are spin- and parity-forbidden, the perovskites likely exhibit forbidden transitions with small dipole transition matrix element and therefore, weak optical absorption coefficients for photons with energies close to the bandgap. However, inversion symmetry-induced parity-forbidden transitions can be relaxed by structural distortions, and spin-forbidden transitions by spin–orbit and magnetic couplings. Symmetry can be broken by varying the steric size of the A cation site and introducing octahedral tilts.¹⁰⁶ It is worth noting that some discrepancies can be found in calculations.^{93,94,107}

As mentioned before, Mn^{II} can be incorporated with full solubility in the previous structures to form new alloys, $\text{Cs}_4\text{Cd}_{1-x}\text{Mn}_x\text{Sb}_2\text{Cl}_{12}$ and $\text{Cs}_4\text{Cd}_{1-x}\text{Mn}_x\text{Bi}_2\text{Cl}_{12}$. Mn^{II} is a highly used dopant in lead halide perovskites and many other hosts because of its highly tunable emission and magnetic properties. When incorporated in Bi/Cd $\langle 111 \rangle$ -oriented perovskites, a very high photoluminescence quantum yield (PLQY) of up to 79.5% can be achieved, a result that was attributed to the effects of quantum confinement and a band alignment that allowed an efficient excitonic energy transfer from host to Mn^{II} centers. This differs from other Mn-doped halide perovskites and nanocrystals (NCs) where the difference in ionic radii limits the incorporation of Mn into the

structures and promotes traps and defects,^{80,108,109} in these materials, alloys with large amounts of Mn can be synthesized, allowing for larger PLQYs.¹⁰¹ Woodward also proposes that the Bi materials can absorb radiation through localized BiCl_6 octahedra where Cd serves to isolate Bi–Mn–Bi networks, decreasing the electronic dimensionality of the materials but increasing radiative recombination in Mn^{II} sites.¹⁰⁵ Replacing Bi by Sb drastically reduces the PLQY to 28.5% (Figure 12B,C), which can be attributed to the reduced spin–orbit coupling in Sb (in comparison to Bi) and the increased electronic dimensionality in the Sb-compounds that negatively affect the energy transfer from the SbCl_6 octahedra to Mn^{II} centers.¹⁰² Conversely, in the absence of Mn centers, the pure Cd materials show a broad emission PL, probably originating from STEs.^{93,110}

The first synthesized inorganic LDP was $\text{Cs}_4\text{CuSb}_2\text{Cl}_{12}$ with a bandgap of around 1.0 eV, which crystallizes in the monoclinic crystal structure $\text{C2}/m$. Unlike the materials described above, the CuCl_6 octahedra are Jahn–Teller distorted, which explains the less symmetric crystal group of the perovskite. The Jahn–Teller distortion lifts the degeneracy of the Cu d states, leading to a separation of the d states and the formation of a low conduction flat band mainly composed of $\text{Cu } d_{x^2-y^2}$ orbitals hybridized with Cl p orbitals. The low dispersive band results in almost equal direct and indirect bandgaps. Moreover, the bandgap can be modulated through dimensional reduction; Cai found a direct bandgap of 1.79 eV for $\text{Cs}_4\text{CuSb}_2\text{Cl}_{12}$ NCs synthesized by a modified hot injection method.⁹¹ Unsurprisingly, NCs have larger bandgaps as a result of quantum confinement. Wang et al. predict a transition from indirect bandgap in bulk samples, to direct bandgap for single layer NCs and improved band dispersion (synthesized by ultrasonic exfoliation).⁹²

Mn^{II} can also be incorporated with full solubility in this Cu^{II} perovskite, but unlike their Cd^{II} analogues, a low-intensity emission from Mn^{II} centers can be observed only for the pure-Mn material while the Cu-containing materials do not exhibit PL emission at room temperature in their powder form. However, Wang et al. were able to measure PL emission at 630 nm in $\text{Cs}_4\text{CuSb}_2\text{Cl}_{12}$ NCs. They proposed an ultrafast charge-trapping process competing with a radiative decay, which results in a weak and broad photoluminescence.⁹² The optical bandgap can be tuned upon Cu incorporation from 3.0 to 1.0 eV for the Mn-only and Cu-only materials, respectively. For

the mixed-metal materials, there is a nonlinear change in bandgap with respect to copper content: upon incorporation of small amounts of copper, the bandgap rapidly decreases, which is indicative of a drastic change in the electronic structure (Figure 12A).¹⁰⁰ Further, the distinct magnetic behavior of $\text{Cs}_4\text{MnSb}_2\text{Cl}_{12}$ and $\text{Cs}_4\text{CuSb}_2\text{Cl}_{12}$ phases allows the modulation of the antiferromagnetic behavior for the mixed-metal phases. Cai et al.⁹¹ were able to integrate the DP $\text{Cs}_2\text{AgSbCl}_6$ with the Cu^{II} layered perovskite in solid solutions of $\text{Cs}_4\text{Cu}_x\text{Ag}_{2-x}\text{Sb}_2\text{Cl}_{12}$ NCs ($0 < x < 1$). By modulating the materials composition, they can modify the crystal structure from cubic to monoclinic layered double perovskite and the corresponding electronic band alignment from indirect to direct bandgap.

Even at this early stage in the development of LDPs, some of them show properties that would allow them to be incorporated into devices such as photodetectors, while others could be attractive for applications in LEDs, solar cells, and ferroelectrics.

Applications of LDPs. The chemical and structural diversity of LDPs bestows them new and intriguing physical and optoelectronic properties. Even at this early stage in the development of LDPs, some materials show properties that would allow them to be incorporated into devices such as photodetectors, while some others could be attractive for applications in LEDs, solar cells, and ferroelectrics. Further, some other applications have been proposed and studied by computational methods.

Solar Cells. One of the most attractive applications for LDPs is as absorbers in solar cells; particularly $\text{Cs}_4\text{CuSb}_2\text{Cl}_{12}$ with a bandgap of 1.0 eV and remarkable stability. However, this perovskite has not been implemented yet in a solar cell, partly because of the difficulties encountered to produce high-quality films of this and related materials. The one-layered ($n = 1$) Ag/Bi LDPs have direct bandgaps between 2.5 and 1.9 eV, which might make them suitable for photovoltaic applications. Unlike their 3D analogues,¹¹¹ or their $\langle 111 \rangle$ -oriented counterparts, $\langle 100 \rangle$ -LDPs can be deposited in high-quality thin films by solution-processable methods (Figure 13A,B). However, low band dispersion usually results in large electron/hole effective masses and thus in low mobilities, which are deleterious for solar cells.⁴² An alternative to overcome this limitation is to replace Ag^{I} with In^{I} or Tl^{I} . Moreover, approaches used in 2D hybrid lead halide perovskites, like the perpendicular alignment between layers and substrate or by the incorporation of conducting polymers as organic motif, could be an interesting avenue to offset conductivity issues of the LDPs.

Ferroelectrics. Another possibility for layered halide perovskites is their use in ferroelectric applications. Their ferroelectric properties come from their structural softness and low synthesis temperatures that allow them to accommodate dynamic polar cations between the inorganic layers.¹¹² The advantage of LDPs with respect to lead halides is that the electronic structure can be further tuned and can be made of elements that are less toxic than lead. Room-temperature ferroelectricity in LDPs was first reported for $(3\text{-CPA})_4\text{AgBiBr}_8$ (Figure 13C). The asymmetric chain ligand 3-CPA^+ greatly influences the formation of a polar structure, which enables a phase transition from an acentric state Pc (ferroelectric phase) to a centrosymmetric state $Pbam$ (paraelectric phase). The Curie–Weiss temperatures are $T_0 = 302$ K and $T_0' = 307$ K for the ferroelectric and paraelectric phases, respectively, and the saturation polarization is $P_s = 3.2$

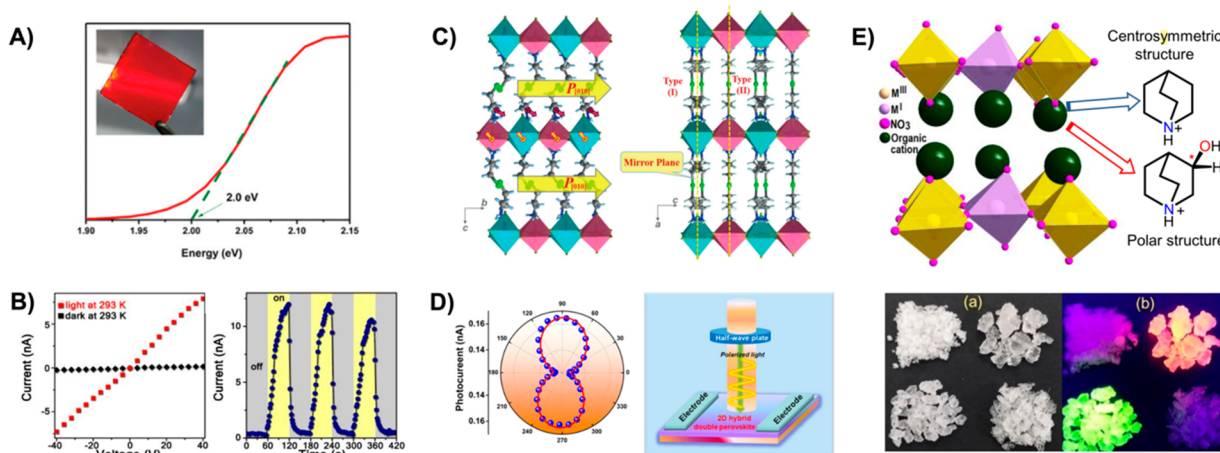


Figure 13. (A) $(3\text{-IPA})_4\text{AgBiI}_8$ has a 2.0 eV bandgap and can be deposited in thin-film form by solution processable deposition techniques, which are promising properties for solar cells.⁴⁷ (B) $(1,4\text{-CyDA})_2\text{AgBiI}_8 \cdot \text{H}_2\text{O}$ presents photoconduction demonstrating the semiconductor nature of the material.⁵² (C) Dipolar interaction between the organic moieties and the inorganic layers enable a phase transition from a non-centrosymmetric group (left) to a symmetric group for $(3\text{-CPA})_4\text{AgBiBr}_8$ (right).⁴⁹ (D) Anisotropy of optical properties in LDPs. For example, $(i\text{-PA})_4\text{AgBiBr}_8$ is promising for polarization-sensitive detectors. Left: Polar plots of the photocurrent under the polarized-light irradiation. Right: Diagram of crystal-device configuration for polarized-light detection.⁵⁰ (E) Chiral molecules transfer their chirality to lanthanide-nitrate multifunctional LDPs (top inset). The use of chiral organic cations R/S -3-hydroxyquinuclidinium leads to formation of ferroelectric chiral crystals (polar structure). The use of lanthanides also enables photoluminescence (bottom image).⁶³ Adapted from (A) ref 47 and (B) ref 52 with permission of the Royal Society of Chemistry. Adapted from (C) ref 49 and (D) ref 50. Copyright 2020 Wiley-VCH Verlag GmbH & Co. KGaA, Weinheim. (E) Adapted from ref 63. Copyright 2020 American Chemical Society.

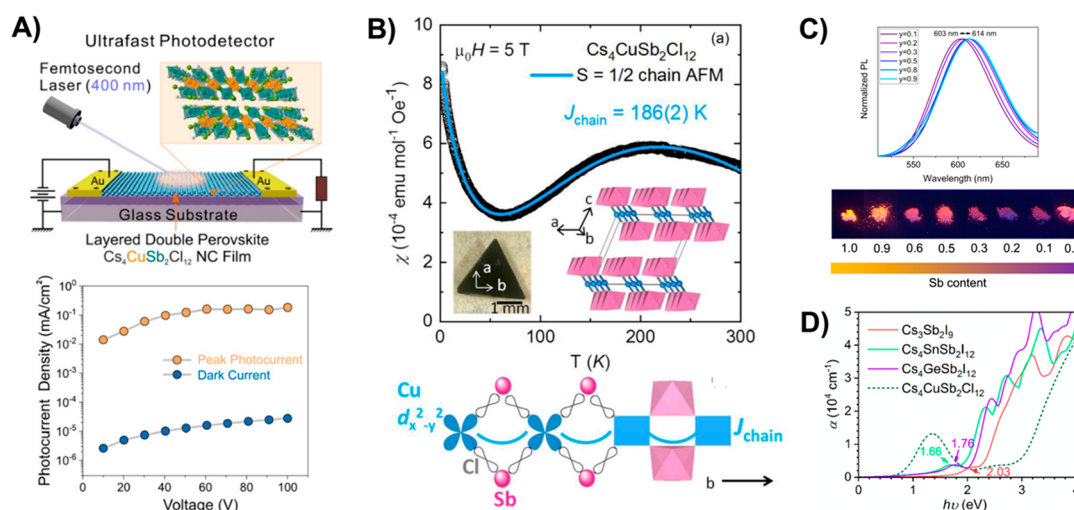


Figure 14. (A) Top: High-speed photodetector device based on $\text{Cs}_4\text{CuSb}_2\text{Cl}_{12}$ NCs. Bottom: The device has an ultrafast photocurrent peak density four-orders of magnitude higher than the dark current density.⁹¹ Copyright 2020 American Chemical Society. (B) (Top) Magnetic susceptibility as a function of temperature of $\text{Cs}_4\text{CuSb}_2\text{Cl}_{12}$ single crystal and (bottom) superexchange interaction along the 1D Cu chains.⁸⁹ Copyright 2020 American Physical Society. (C) Emission tuning from Sb/Bi/Cd Mn^{2+} alloys that could be used for LED or phosphors applications.¹⁰² (D) Calculated absorption spectra of $\text{Cs}_3\text{Sb}_2\text{I}_9$, $\text{Cs}_4\text{SnSb}_2\text{I}_{12}$, $\text{Cs}_4\text{GeSb}_2\text{I}_{12}$, and $\text{Cs}_4\text{CuSb}_2\text{Cl}_{12}$. The incorporation of divalent Ge and Sn in iodide (111)-LDPs could drastically improve absorption.^{104,119} Copyright 2018 American Chemical Society.

$\mu\text{C cm}^{-2}$ at room temperature.⁴⁹ Ferroelectric polarization in LDPs is also possible using a symmetric organic cation like PA^+ . For the two-layered $\text{PA}_2\text{CsAgBiBr}_7$, the spontaneous polarization at ca. 200 K ($P_s = 1.5 \mu\text{C cm}^{-2}$) arises from the collective effects of an order–disorder transition of the organic moieties and the atomic displacement of inorganic cesium cations.⁵¹ While decent values, these are still far from those of recently reported molecular ferroelectrics (for example MDABCO– NH_4I_3 , with an estimated P_s value at 373 K of $19 \mu\text{C cm}^{-2}$).¹¹³ One way to potentially improve the ferroelectric performance is through the incorporation of chiral organic ligands.^{67,114} Indeed, this has been successfully demonstrated in related nitrate– NO_3 LDPs, $(\text{S3HQ})_4\text{KCe}(\text{NO}_3)_8$ and $(\text{R3HQ})_4\text{KCe}(\text{NO}_3)_8$, where R3HQ and S3HQ stand for R- and S-hydroxylquinuclidinium respectively (Figure 13E).⁶³

Photodetectors. Layered perovskites are particularly promising materials for photodetection because of their highly anisotropic structure that combines intrawell charge conductive channels and resistive hopping barriers in orthogonal orientations.³² In 2019, Xu et al. demonstrated the X-ray detecting capability of $\text{BA}_2\text{CsAgBiBr}_7$. Single crystals of the material exhibited a charge collection efficiency, given by the mobility–lifetime product ($\mu\tau$) of $1.21 \times 10^{-3} \text{ cm}^2\text{V}^{-1}$, and the fabricated detector exhibited a promising sensitivity of $4.2 \mu\text{C mGy}_{\text{air}}^{-1} \text{ cm}^{-2}$ (Figure 13B).⁵³ More recently, $(3\text{-CPA})_4\text{AgBiBr}_8$ LDP single crystals showed a mobility–lifetime product of $\mu\tau = 1.0 \times 10^{-3} \text{ cm}^2\text{V}^{-1}$.⁴⁹ Remarkably, $\mu\tau$ in both LDPs are higher than that of sintered hybrid lead triiodide perovskite wafers,¹¹⁵ perovskite films,⁵ or $\text{Cs}_2\text{AgBiBr}_6$ single-crystal X-ray detectors.¹¹⁶ In layered lead perovskites, detector sensitivity was enhanced through ferroelectricity,¹¹⁷ a method that could translate to LDPs as well. The anisotropic nature of the layered LDPs could be applied in polarization-sensitive photodetectors (Figure 13D), as proposed by Li using the $(i\text{-PA})_2\text{CsAgBiBr}_7$ LDP⁵⁰ and in photodetectors as proposed by Jayasankar with the $\text{Cs}_4\text{CuSb}_2\text{Cl}_{12}$ perovskite.¹¹⁸

Spintronics. Inorganic LDPs multifunctional magnetic/luminescent perovskites are promising materials for applications in spin-electronics, spin-photonics, and LEDs.¹²⁰ For example, $\text{Cs}_4\text{MnSb}_2\text{Cl}_{12}$ and $\text{Cs}_4\text{MnBi}_2\text{Cl}_{12}$ show an anti-ferromagnetic behavior due to superexchange interactions that follows the Curie–Weiss law.¹⁰⁰ The magnetic superexchange interaction of the Cu^{2+} centers in $\text{Cs}_4\text{CuSb}_2\text{Cl}_{12}$ further expands the possible applications of inorganic LDPs. Recently, Tran and co-workers showed that $\text{Cs}_4\text{CuSb}_2\text{Cl}_{12}$ is a 1/2 Heisenberg antiferromagnetic chain that could stabilize a quantum spin liquid over a wide temperature window (Figure 14B).⁸⁹ In addition to magnetic interactions, LDPs with formula $\text{Cs}_4\text{Cd}_{1-x}\text{Mn}_x\text{B}^{\text{III}}\text{Cl}_{12}$ ($\text{B} = \text{Sb}, \text{Bi}$) display photoluminescence that can be tuned and can be utilized in photoluminescence applications (Figure 14C).¹⁰² The substitution of the B^{III} or B^{II} metals by lanthanides,¹²¹ alkaline earth cations,¹²² or other divalent transition metals¹²³ could lead to interesting emission properties such as upconversion¹²⁴ and downshifting.¹²⁵ Yet another important avenue of research is to explore the downscaling of LDPs to the nanoregime and try to harness the quantum effects.^{126,127} This has been recently achieved for $\text{Cs}_4\text{CuSb}_2\text{Cl}_{12}$ and the resulting nanocrystals employed in high-speed photodetectors (Figure 14A).

Computational efforts have also attempted to find or predict other applications for LDPs. For example, some have speculated that (111)-oriented $\text{Cs}_4\text{CdSb}_2\text{Cl}_{12}$ could be a suitable p-type transparent conductor.⁹⁴ Although these claims have been disputed,^{128,129} the possibility to develop new transparent conducting materials is potentially very attractive. Others have predicted that some of these materials could have suitable properties for their applications in solar cells (Figure 14D)¹¹⁹ or present half-metallicity,³⁵ or that they could be used for the fabrication of vertical and lateral heterostructures.¹³⁰

We also believe that the LDPs could be used as photocatalysts because of the possibilities of tuning the bandgap and the variety of cations that can be used.^{131,132} However, suitable combinations of cations or dopants need to

be explored to offset issues that can limit their uses in some applications like solar cells and LEDs. Also, reengineering approaches already implemented in 2D lead halide and 3D double perovskites will be necessary to enhance the physical properties or device functions of LDPs, for example, passivation,¹³³ defects engineering,¹³⁴ layer orientation,¹³⁵ and doping,⁸⁵ among others.

Perspectives and Conclusions. In this Focus Review, we summarized the structural, optical, and electronic effects of cations' permutation in layered perovskites. The transmutation of divalent cations, such as lead Pb^{II} , into combinations of B^{I} , B^{II} , and B^{III} cations, leads to the formation of layered double perovskites, with large organic ammonium cations or vacancy sites as lattice separators. The ability to include cations in several oxidation states and their permutations widens the chemical space of layered perovskites and perovskites in general tremendously; this results in an immense number of possible materials with lower toxicity and improved stability in comparison to lead halide perovskites.

While to date only a handful of halide LDPs are known, the existing ones have shown a wide range of properties and applications, ranging from solar cells to ferroelectrics and light-emitting materials (Figure 15). We envision future research to

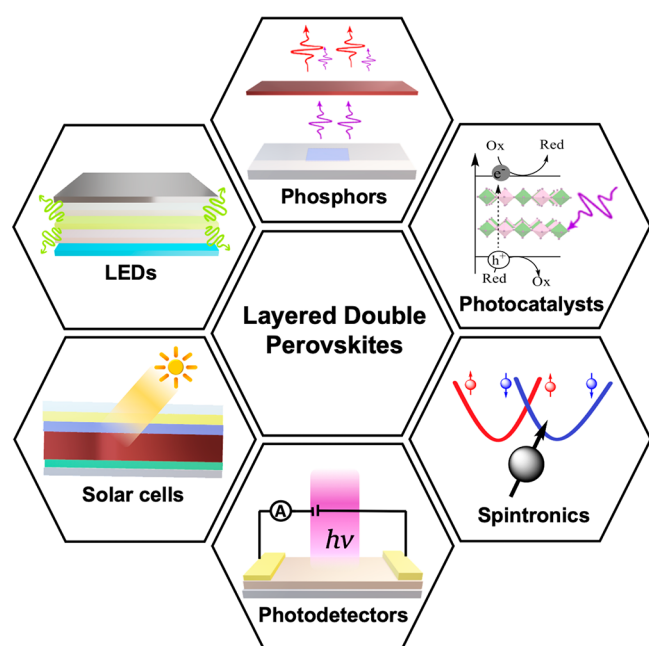


Figure 15. Possible applications of LDPs. In the clockwise direction: phosphors, photocatalysts, spintronics, photodetectors, solar cells, and light-emitting devices. Out of these, photodetectors and ferroelectric properties have been reported for $\langle 100 \rangle$ -LDPs.^{49–51,53} For $\langle 111 \rangle$ -oriented LDPs, PLQYs of up to 79.5% could be incorporated in light-emitting devices as phosphor or active layer in LEDs.^{101,102} The magnetic properties of Mn^{II} or Cu^{II} in these perovskites could also be harnessed for spintronic applications.^{89,101,102,105}

widen the applications of LDPs, for example, incorporation of chiral cations, chromophores, or thermochromic and magnetic metallic cations should uncover exciting phenomena that can enhance the importance of LDPs. Also, the possibility to employ these materials as transparent conductors or photocatalysts could be an exciting avenue.

Despite significant advances, the field is still at a very early stage and, as such, there are still plenty of unknowns yet to be investigated. For example, work still needs to be done to develop better guidelines to design the chemical and electronic structure of the LDPs. Also, further exploration of possible metals and cations that can be incorporated in LDPs will be crucial for the field in the upcoming years and will determine the true potential of this novel family of materials.

■ ASSOCIATED CONTENT

Supporting Information

The Supporting Information is available free of charge at <https://pubs.acs.org/doi/10.1021/acsenerylett.0c01867>.

Compilation of reported halide (and nitrate) LDPs and some of their properties (Table S1) (PDF)

■ AUTHOR INFORMATION

Corresponding Author

Diego Solis-Ibarra — Laboratorio de Físicoquímica y Reactividad de Superficies (LaFREs), Instituto de Investigaciones en Materiales, Universidad Nacional Autónoma de México, Coyoacán CDMX 04510, México; orcid.org/0000-0002-2486-0967; Email: diego.solis@unam.mx; <https://www.iim.unam.mx/diegosolis/>

Authors

Brenda Vargas — Laboratorio de Físicoquímica y Reactividad de Superficies (LaFREs), Instituto de Investigaciones en Materiales, Universidad Nacional Autónoma de México, Coyoacán CDMX 04510, México

Germán Rodríguez-López — Laboratorio de Físicoquímica y Reactividad de Superficies (LaFREs), Instituto de Investigaciones en Materiales, Universidad Nacional Autónoma de México, Coyoacán CDMX 04510, México

Complete contact information is available at: <https://pubs.acs.org/doi/10.1021/acsenerylett.0c01867>

Author Contributions

[§]These authors contributed equally to this work.

Notes

The authors declare no competing financial interest.

Biographies

Brenda Vargas received her Master's (2014) in Material Science and Engineering, working on solid oxide fuel cells. For her Ph.D. she joined Prof. Solis-Ibarra's group (2015) at the Materials Research Institute from UNAM to develop new layered double halide perovskites for optoelectronic applications.

Germán Rodríguez-López received his Ph.D. in Chemistry (2017) at Cinvestav under the tutelage of Prof. Angelina Flores-Parra, working on carbenes and main group chemistry. He then joined Solis-Ibarra's group as a postdoctoral fellow (2018–2020). His research addresses the design of organic ligands for hybrid perovskites and their physical and chemical effects.

Diego Solis-Ibarra received his bachelor's and Ph.D. from UNAM. During this time, he also was an exchange student at UC Santa Barbara and a research intern at MIT. Diego then moved to Stanford University as a postdoctoral researcher. In 2015 he returned to UNAM, where he leads a research group that focuses on developing new materials for photovoltaic and optoelectronic applications.

ACKNOWLEDGMENTS

We acknowledge the financial support from PAPIIT IN216020 and CONACYT's CB-A1-S-8729. We are also grateful to Prof. Karunadasa and B. A. Connor for providing us with high-resolution images for Figure 7 and to P. Carmona-Monroy for assistance with Figure 2.

ACRONYMS AND ABBREVIATIONS

1,4-CyDA, Cyclohexane-1,4-diammonium
 3-BPA, 3-Bromopropylammonium
 3-CPA, 3-Chloropropylammonium
 3-IPA, 3-Iodopropylammonium
 AE2T, 5,5'-diylbis(aminoethyl)-[2,2'-bithiophene]
 AFM, Antiferromagnetic
 BA, Butylammonium
 BDA, Butane-1,4-diammonium
 CBM, Conduction band minimum
 CT, Charge transfer
 DFT, Density functional theory
 DJ, Dion–Jacobson
 DPs, Double perovskites
 FA, Formamidinium
 HIS, Histammonium
 HpDA, Heptane-1,7-diammonium
 I_{eq}, Equatorial iodine
 i-PA, Iso-pentylammonium
 LEDs, Light-emitting diodes
 LDPs, Layered double perovskites
 MA, Methylammonium
 MMCT, Metal-to-metal charge transfer
 $\mu\tau$, Mobility–lifetime product
 μ_{eff} , Effective octahedral factor
 NCs, Nanocrystals
 OcDA, Octane-1,8-diammonium
 PA, Propylammonium
 PCE, Power conversion efficiency
 PEA, Phenethylammonium
 PL, Photoluminescence
 PLQY, Photoluminescence quantum yield
 P_s, Saturation polarization
 R3HQ, (R)-3-Hydroxyl quinuclidinium
 RP, Ruddlesden–Popper
 S3HQ, (S)-3-Hydroxyl quinuclidinium
 STEs, Self-trapped excitons
 t_{eff}, Effective tolerance factor
 VBM, Valence band maximum

REFERENCES

- (1) The National Renewable Energy Laboratory (NREL). <https://www.nrel.gov/pv/assets/pdfs/best-research-cell-efficiencies.20200925.pdf> (2020-10-05).
- (2) Tang, B.; Dong, H.; Sun, L.; Zheng, W.; Wang, Q.; Sun, F.; Jiang, X.; Pan, A.; Zhang, L. Single-Mode Lasers Based on Cesium Lead Halide Perovskite Submicron Spheres. *ACS Nano* **2017**, *11*, 10681–10688.
- (3) Chin, X. Y.; Cortecchia, D.; Yin, J.; Bruno, A.; Soci, C. Lead Iodide Perovskite Light-Emitting Field-Effect Transistor. *Nat. Commun.* **2015**, *6*, 7383.
- (4) Senanayak, S. P.; Yang, B.; Thomas, T. H.; Giesbrecht, N.; Huang, W.; Gann, E.; Nair, B.; Goedel, K.; Guha, S.; Moya, X.; McNeill, C. R.; Docampo, P.; Sadhanala, A.; Friend, R. H.; Sirringhaus, H. Understanding Charge Transport in Lead Iodide Perovskite Thin-Film Field-Effect Transistors. *Sci. Adv.* **2017**, *3*, No. e1601935.
- (5) Yakunin, S.; Sytnyk, M.; Kriegner, D.; Shrestha, S.; Richter, M.; Matt, G. J.; Azimi, H.; Brabec, C. J.; Stangl, J.; Kovalenko, M. V.; Heiss, W. Detection of X-Ray Photons by Solution-Processed Lead Halide Perovskites. *Nat. Photonics* **2015**, *9*, 444–449.
- (6) Park, S.; Chang, W. J.; Lee, C. W.; Park, S.; Ahn, H. Y.; Nam, K. T. Photocatalytic Hydrogen Generation from Hydriodic Acid Using Methylammonium Lead Iodide in Dynamic Equilibrium with Aqueous Solution. *Nat. Energy* **2017**, *2*, 16185.
- (7) Yin, W. J.; Shi, T.; Yan, Y. Unique Properties of Halide Perovskites as Possible Origins of the Superior Solar Cell Performance. *Adv. Mater.* **2014**, *26*, 4653–4658.
- (8) Manser, J. S.; Christians, J. A.; Kamat, P. V. Intriguing Optoelectronic Properties of Metal Halide Perovskites. *Chem. Rev.* **2016**, *116*, 12956–13008.
- (9) Straus, D. B.; Guo, S.; Abeykoon, A. M.; Cava, R. J. Understanding the Instability of the Halide Perovskite CsPbI₃ through Temperature-Dependent Structural Analysis. *Adv. Mater.* **2020**, *32*, 2001069.
- (10) Li, J.; Cao, H. L.; Jiao, W.-B.; Wang, Q.; Wei, M.; Cantone, I.; Lü, J.; Abate, A. Biological Impact of Lead from Halide Perovskites Reveals the Risk of Introducing a Safe Threshold. *Nat. Commun.* **2020**, *11*, 310.
- (11) Hao, F.; Stoumpos, C. C.; Cao, D. H.; Chang, R. P. H.; Kanatzidis, M. G. Lead-Free Solid-State Organic-Inorganic Halide Perovskite Solar Cells. *Nat. Photonics* **2014**, *8*, 489–494.
- (12) Noel, N. K.; Stranks, S. D.; Abate, A.; Wehrenfennig, C.; Guarnera, S.; Haghighirad, A. A.; Sadhanala, A.; Eperon, G. E.; Pathak, S. K.; Johnston, M. B.; Petrozza, A.; Herz, L. M.; Snaith, H. J. Lead-Free Organic-Inorganic Tin Halide Perovskites for Photovoltaic Applications. *Energy Environ. Sci.* **2014**, *7*, 3061–3068.
- (13) Nishimura, K.; Kamarudin, M. A.; Hirotsu, D.; Hamada, K.; Shen, Q.; Iikubo, S.; Minemoto, T.; Yoshino, K.; Hayase, S. Lead-Free Tin-Halide Perovskite Solar Cells with 13% Efficiency. *Nano Energy* **2020**, *74*, 104858.
- (14) Liao, Y.; Liu, H.; Zhou, W.; Yang, D.; Shang, Y.; Shi, Z.; Li, B.; Jiang, X.; Zhang, L.; Quan, L. N.; Quintero-Bermudez, R.; Sutherland, B. R.; Mi, Q.; Sargent, E. H.; Ning, Z. Highly Oriented Low-Dimensional Tin Halide Perovskites with Enhanced Stability and Photovoltaic Performance. *J. Am. Chem. Soc.* **2017**, *139*, 6693–6699.
- (15) Noel, N. K.; Abate, A.; Stranks, S. D.; Parrott, E. S.; Burlakov, V. M.; Goriely, A.; Snaith, H. J. Enhanced Photoluminescence and Solar Cell Performance via Lewis Base Passivation of Organic-Inorganic Lead Halide Perovskites. *ACS Nano* **2014**, *8*, 9815–9821.
- (16) Abdi-Jalebi, M.; Andaji-Garmaroudi, Z.; Cacovich, S.; Stavrakas, C.; Philippe, B.; Richter, J. M.; Alsari, M.; Booker, E. P.; Hutter, E. M.; Pearson, A. J.; Lilliu, S.; Savenije, T. J.; Rensmo, H.; Divitini, G.; Ducati, C.; Friend, R. H.; Stranks, S. D. Maximizing and Stabilizing Luminescence from Halide Perovskites with Potassium Passivation. *Nature* **2018**, *555*, 497–501.
- (17) Cortecchia, D.; Dewi, H. A.; Yin, J.; Bruno, A.; Chen, S.; Baikie, T.; Boix, P. P.; Grätzel, M.; Mhaisalkar, S.; Soci, C.; Mathews, N. Lead-Free MA₂CuCl_xBr_{4-x} Hybrid Perovskites. *Inorg. Chem.* **2016**, *55*, 1044–1052.
- (18) Giustino, F.; Snaith, H. J. Toward Lead-Free Perovskite Solar Cells. *ACS Energy Lett.* **2016**, *1*, 1233–1240.
- (19) Igbari, F.; Wang, Z. K.; Liao, L. S. Progress of Lead-Free Halide Double Perovskites. *Adv. Energy Mater.* **2019**, *9*, 1803150.
- (20) Wang, Z.; Lin, Q.; Chmiel, F. P.; Sakai, N.; Herz, L. M.; Snaith, H. J. Efficient Ambient-Air-Stable Solar Cells with 2D-3D Heterostructured Butylammonium-Cesium-Formamidinium Lead Halide Perovskites. *Nat. Energy* **2017**, *2*, 17135.
- (21) Wygant, B. R.; Ye, A. Z.; Dolocan, A.; Vu, Q.; Abbot, D. M.; Mullins, C. B. Probing the Degradation Chemistry and Enhanced Stability of 2D Organolead Halide Perovskites. *J. Am. Chem. Soc.* **2019**, *141*, 18170–18181.
- (22) Smith, I. C.; Hoke, E. T.; Solis-Ibarra, D.; McGehee, M. D.; Karunadasa, H. I. A Layered Hybrid Perovskite Solar-Cell Absorber with Enhanced Moisture Stability. *Angew. Chem., Int. Ed.* **2014**, *53*, 11232–11235.

- (23) Liu, Y.; Akin, S.; Pan, L.; Uchida, R.; Arora, N.; Milić, J. V.; Hinderhofer, A.; Schreiber, F.; Uhl, A. R.; Zakeeruddin, S. M.; Hagfeldt, A.; Ibrahim Dar, M.; Grätzel, M. Ultrahydrophobic 3D/2D Fluoroarene Bilayer-Based Water-Resistant Perovskite Solar Cells with Efficiencies Exceeding 22%. *Sci. Adv.* **2019**, *5*, No. eaaw2543.
- (24) Grancini, G.; Roldán-Carmona, C.; Zimmermann, I.; Mosconi, E.; Lee, X.; Martineau, D.; Nabey, S.; Oswald, F.; De Angelis, F.; Graetzel, M.; Nazeeruddin, M. K. One-Year Stable Perovskite Solar Cells by 2D/3D Interface Engineering. *Nat. Commun.* **2017**, *8*, 15684.
- (25) Ortiz-Cervantes, C.; Carmona-Monroy, P.; Solis-Ibarra, D. Two-Dimensional Halide Perovskites in Solar Cells: 2D or Not 2D? *ChemSusChem* **2019**, *12*, 1560–1575.
- (26) Ortiz-Cervantes, C.; Román-Román, P. I.; Vazquez-Chavez, J.; Hernández-Rodríguez, M.; Solis-Ibarra, D. Thousand-Fold Conductivity Increase in 2D Perovskites by Polydiacetylene Incorporation and Doping. *Angew. Chem., Int. Ed.* **2018**, *57*, 13882–13886.
- (27) Mao, L.; Stoumpos, K. C.; Kanatzidis, M. G. Two-Dimensional Hybrid Halide Perovskites: Principles and Promises. *J. Am. Chem. Soc.* **2019**, *141*, 1171–1190.
- (28) Katan, C.; Mercier, N.; Even, J. Quantum and Dielectric Confinement Effects in Lower-Dimensional Hybrid Perovskite Semiconductors. *Chem. Rev.* **2019**, *119*, 3140–3192.
- (29) Stoumpos, C. C.; Cao, D. H.; Clark, D. J.; Young, J.; Rondinelli, J. M.; Jang, J. I.; Hupp, J. T.; Kanatzidis, M. G. Ruddlesden-Popper Hybrid Lead Iodide Perovskite 2D Homologous Semiconductors. *Chem. Mater.* **2016**, *28*, 2852–2867.
- (30) Yuan, M.; Quan, L. N.; Comin, R.; Walters, G.; Sabatini, R.; Voznyy, O.; Hoogland, S.; Zhao, Y.; Beauregard, E. M.; Kanjanaboos, P.; Lu, Z.; Kim, D. H.; Sargent, E. H. Perovskite Energy Funnels for Efficient Light-Emitting Diodes. *Nat. Nanotechnol.* **2016**, *11*, 872–877.
- (31) Raghavan, C. M.; Chen, T. P.; Li, S. S.; Chen, W. L.; Lo, C. Y.; Liao, Y. M.; Haider, G.; Lin, C. C.; Chen, C. C.; Sankar, R.; Chang, Y. M.; Chou, F. C.; Chen, C. W. Low-Threshold Lasing from 2D Homologous Organic-Inorganic Hybrid Ruddlesden-Popper Perovskite Single Crystals. *Nano Lett.* **2018**, *18*, 3221–3228.
- (32) Feng, J.; Gong, C.; Gao, H.; Wen, W.; Gong, Y.; Jiang, X.; Zhang, B.; Wu, Y.; Wu, Y.; Fu, H.; Jiang, L.; Zhang, X. Single-Crystalline Layered Metal-Halide Perovskite Nanowires for Ultra-sensitive Photodetectors. *Nat. Electron.* **2018**, *1*, 404–410.
- (33) Mak, K. F.; Lee, C.; Hone, J.; Shan, J.; Heinz, T. F. Atomically Thin MoS₂: A New Direct-Gap Semiconductor. *Phys. Rev. Lett.* **2010**, *105*, 136805.
- (34) Vargas, B.; Ramos, E.; Pérez-Gutiérrez, E.; Alonso, J. C.; Solis-Ibarra, D. A Direct Bandgap Copper-Antimony Halide Perovskite. *J. Am. Chem. Soc.* **2017**, *139*, 9116–9119.
- (35) Xu, J.; Xu, C.; Liu, J.-B.; et al. Prediction of Room-Temperature Half-Metallicity in Layered Halide Double Perovskites. *npj Comput. Mater.* **2019**, *5*, 114.
- (36) Castro-Castro, L.; Guloy, A. Organic-Based Layered Perovskites of Mixed-Valent Gold(I)/Gold(III) Iodides. *Angew. Chem.* **2003**, *115*, 2877–2880.
- (37) Wells, H. L. Some Complex Chlorides Containing Gold. III. A New Cesium-Auric Chloride. *Am. J. Sci.* **1922**, *44*, 414–416.
- (38) Connor, B. A.; Leppert, L.; Smith, M. D.; Neaton, J. B.; Karunadasa, H. I. Layered Halide Double Perovskites: Dimensional Reduction of Cs₂AgBiBr₆. *J. Am. Chem. Soc.* **2018**, *140*, 5235–5240.
- (39) Slavney, A. H.; Hu, T.; Lindenberg, A. M.; Karunadasa, H. I. A Bismuth-Halide Double Perovskite with Long Carrier Recombination Lifetime for Photovoltaic Applications. *J. Am. Chem. Soc.* **2016**, *138*, 2138–2141.
- (40) Gao, W.; Ran, C.; Xi, J.; Jiao, B.; Zhang, W.; Wu, M.; Hou, X.; Wu, Z. High-Quality Cs₂AgBiBr₆ Double Perovskite Film for Lead-Free Inverted Planar Heterojunction Solar Cells with 2.2% Efficiency. *ChemPhysChem* **2018**, *19*, 1696–1700.
- (41) Greul, E.; Petrus, M. L.; Binek, A.; Docampo, P.; Bein, T. Highly Stable, Phase Pure Cs₂AgBiBr₆ Double Perovskite Thin Films for Optoelectronic Applications. *J. Mater. Chem. A* **2017**, *5*, 19972–19981.
- (42) Longo, G.; Mahesh, S.; Buizza, L. R. V.; Wright, A. D.; Ramadan, A. J.; Abdi-Jalebi, M.; Nayak, P. K.; Herz, L. M.; Snaith, H. J. Understanding the Performance-Limiting Factors of Cs₂AgBiBr₆ Double-Perovskite Solar Cells. *ACS Energy Lett.* **2020**, *5*, 2200–2207.
- (43) Jana, M. K.; Janke, S. M.; Dirkes, D. J.; Dovletgeldi, S.; Liu, C.; Qin, X.; Gundogdu, K.; You, W.; Blum, V.; Mitzi, D. B. Direct-Bandgap 2D Silver-Bismuth Iodide Double Perovskite: The Structure-Directing Influence of an Oligothiophene Spacer Cation. *J. Am. Chem. Soc.* **2019**, *141*, 7955–7964.
- (44) Fang, Y.; Zhang, L.; Wu, L.; Yan, J.; Lin, Y.; Wang, K.; Mao, W. L.; Zou, B. Pressure-Induced Emission (PIE) and Phase Transition of a Two-Dimensional Halide Double Perovskite (BA)₄AgBiBr₈ (BA = CH₃(CH₂)₃NH₃⁺). *Angew. Chem., Int. Ed.* **2019**, *58*, 15249–15253.
- (45) McClure, E. T.; McCormick, A. P.; Woodward, P. M. Four Lead-Free Layered Double Perovskites with the n = 1 Ruddlesden-Popper Structure. *Inorg. Chem.* **2020**, *59*, 6010–6017.
- (46) Mao, L.; Teicher, S. M. L.; Stoumpos, C. C.; Kennard, R. M.; Decrescent, R. A.; Wu, G.; Schuller, J. A.; Chabiny, M. L.; Cheetham, A. K.; Seshadri, R. Chemical and Structural Diversity of Hybrid Layered Double Perovskite Halides. *J. Am. Chem. Soc.* **2019**, *141*, 19099–19109.
- (47) Yao, Y.; Kou, B.; Peng, Y.; Wu, Z.; Li, L.; Wang, S.; Zhang, X.; Liu, X.; Luo, J. (C₃H₉NI)₄AgBiI₈: A Direct-Bandgap Layered Double Perovskite Based on a Short-Chain Spacer Cation for Light Absorption. *Chem. Commun.* **2020**, *56*, 3206–3209.
- (48) Lassoued, M. S.; Bi, L. Y.; Wu, Z.; Zhou, G.; Zheng, Y. Z. Piperidine-Induced Switching of the Direct Band Gaps of Ag(I)/Bi(III) Bimetallic Iodide Double Perovskites. *J. Mater. Chem. C* **2020**, *8*, 5349–5354.
- (49) Guo, W.; Liu, X.; Han, S.; Liu, Y.; Xu, Z.; Hong, M.; Luo, J.; Sun, Z. Room-Temperature Ferroelectric Material Composed of a Two-Dimensional Metal Halide Double Perovskite for X-ray Detection. *Angew. Chem.* **2020**, *132*, 13983–13988.
- (50) Li, Y.; Yang, T.; Xu, Z.; Liu, X.; Huang, X.; Han, S.; Liu, Y.; Li, M.; Luo, J.; Sun, Z. Dimensional Reduction of Cs₂AgBiBr₆: A 2D Hybrid Double Perovskite with Strong Polarization Sensitivity. *Angew. Chem.* **2020**, *132*, 3457–3461.
- (51) Zhang, W.; Hong, M.; Luo, J. Halide Double Perovskite Ferroelectrics. *Angew. Chem., Int. Ed.* **2020**, *59*, 9305–9308.
- (52) Bi, L. Y.; Hu, Y. Q.; Li, M. Q.; Hu, T. L.; Zhang, H. L.; Yin, X. T.; Que, W. X.; Lassoued, M. S.; Zheng, Y. Z. Two-Dimensional Lead-Free Iodide-Based Hybrid Double Perovskites: Crystal Growth, Thin-Film Preparation and Photocurrent Responses. *J. Mater. Chem. A* **2019**, *7*, 19662–19667.
- (53) Xu, Z.; Liu, X.; Li, Y.; Liu, X.; Yang, T.; Ji, C.; Han, S.; Xu, Y.; Luo, J.; Sun, Z. Exploring Lead-Free Hybrid Double Perovskite Crystals of (BA)₂CsAgBiBr₇ with Large Mobility-Lifetime Product toward X-Ray Detection. *Angew. Chem., Int. Ed.* **2019**, *58*, 15757–15761.
- (54) Connor, B. A.; Biega, R.-I.; Leppert, L.; Karunadasa, H. I. Dimensional Reduction of the Small-Bandgap Double Perovskite Cs₂AgTiBr₆. *Chem. Sci.* **2020**, *11*, 7708–7715.
- (55) Fox, B. S.; Beyer, M. K.; Bondybey, V. E. Coordination Chemistry of Silver Cations. *J. Am. Chem. Soc.* **2002**, *124*, 13613–13623.
- (56) Ruddlesden, S. N.; Popper, P. The Compound Sr₃Ti₂O₇ and Its Structure. *Acta Crystallogr.* **1958**, *11*, 54–55.
- (57) Nirala, G.; Yadav, D.; Upadhyay, S. Ruddlesden-Popper Phase A₂BO₄ Oxides: Recent Studies on Structure, Electrical, Dielectric, and Optical Properties. *J. Adv. Ceram.* **2020**, *9*, 129–148.
- (58) Li, J.; Yu, Q.; He, Y.; Stoumpos, C. C.; Niu, G.; Kanatzidis, M. G.; et al. Cs₂PbI₂Cl₂, All-Inorganic Two-Dimensional Ruddlesden-Popper Mixed Halide Perovskite with Optoelectronic Response. *J. Am. Chem. Soc.* **2018**, *140*, 11085–11090.
- (59) Volonakis, G.; Haghighirad, A. A.; Milot, R. L.; Sio, W. H.; Filip, M. R.; Wenger, B.; Johnston, M. B.; Herz, L. M.; Snaith, H. J.; Giustino, F. Cs₂InAgCl₆: A New Lead-Free Halide Double Perovskite with Direct Band Gap. *J. Phys. Chem. Lett.* **2017**, *8*, 772–778.

- (60) Bi, L. Y.; Hu, T. L.; Li, M. Q.; Ling, B. K.; Lassoued, M. S.; Hu, Y. Q.; Wu, Z.; Zhou, G.; Zheng, Y. Z. Template Effects in Cu(I)-Bi(III) Iodide Double Perovskites: A Study of Crystal Structure, Film Orientation, Band Gap and Photocurrent Response. *J. Mater. Chem. A* **2020**, *8*, 7288–7296.
- (61) Xiao, Z.; Du, K. Z.; Meng, W.; Mitzi, D. B.; Yan, Y. Chemical Origin of the Stability Difference between Copper(I)- and Silver(I)-Based Halide Double Perovskites. *Angew. Chem., Int. Ed.* **2017**, *56*, 12107–12111.
- (62) Batsanov, S. S. Van Der Waals Radii of Elements. *Inorg. Mater.* **2001**, *37*, 871–885.
- (63) Shi, C.; Ye, L.; Gong, Z. X.; Ma, J. J.; Wang, Q. W.; Jiang, J. Y.; Hua, M. M.; Wang, C. F.; Yu, H.; Zhang, Y.; Ye, H. Y. Two-Dimensional Organic-Inorganic Hybrid Rare-Earth Double Perovskite Ferroelectrics. *J. Am. Chem. Soc.* **2020**, *142*, 545–551.
- (64) Shi, C.; Ma, J.-J.; Jiang, J.-Y.; Hua, M.-M.; Xu, Q.; Yu, H.; Zhang, Y.; Ye, H.-Y. Large Piezoelectric Response in Hybrid Rare-Earth Double Perovskite Relaxor Ferroelectrics. *J. Am. Chem. Soc.* **2020**, *142*, 9634–9641.
- (65) Smith, M. D.; Jaffe, A.; Dohner, E. R.; Lindenberg, A. M.; Karunadasa, H. I. Structural Origins of Broadband Emission from Layered Pb-Br Hybrid Perovskites. *Chem. Sci.* **2017**, *8*, 4497–4504.
- (66) Gao, X.; Zhang, X.; Yin, W.; Wang, H.; Hu, Y.; Zhang, Q.; Shi, Z.; Colvin, V. L.; Yu, W. W.; Zhang, Y. Ruddlesden-Popper Perovskites: Synthesis and Optical Properties for Optoelectronic Applications. *Adv. Sci.* **2019**, *6*, 1900941.
- (67) Long, G.; Sabatini, R.; Saidaminov, M. I.; Lakhwani, G.; Rasmita, A.; Liu, X.; Sargent, E. H.; Gao, W. Chiral-Perovskite Optoelectronics. *Nat. Rev. Mater.* **2020**, *5*, 423–439.
- (68) Trujillo-Hernández, K.; Rodríguez-López, G.; Espinosa-Roa, A.; González-Roque, J.; Gómora-Figueroa, A. P.; Zhang, W.; Halasyamani, P. S.; Jancik, V.; Gembicky, M.; Pirruccio, G.; Solis-Ibarra, D. Chirality Control in White-Light Emitting 2D Perovskites. *J. Mater. Chem. C* **2020**, *8*, 9602–9607.
- (69) Smith, M. D.; Connor, B. A.; Karunadasa, H. I. Tuning the Luminescence of Layered Halide Perovskites. *Chem. Rev.* **2019**, *119*, 3104–3139.
- (70) Xiao, Z.; Song, Z.; Yan, Y. From Lead Halide Perovskites to Lead-Free Metal Halide Perovskites and Perovskite Derivatives. *Adv. Mater.* **2019**, *31*, 1803792.
- (71) Zhao, X. G.; Yang, D.; Ren, J. C.; Sun, Y.; Xiao, Z.; Zhang, L. Rational Design of Halide Double Perovskites for Optoelectronic Applications. *Joule* **2018**, *2*, 1662–1673.
- (72) Savory, C. N.; Walsh, A.; Scanlon, D. O. Can Pb-Free Halide Double Perovskites Support High-Efficiency Solar Cells? *ACS Energy Lett.* **2016**, *1*, 949–955.
- (73) Maughan, A. E.; Ganose, A. M.; Scanlon, D. O.; Neilson, J. R. Perspectives and Design Principles of Vacancy-Ordered Double Perovskite Halide Semiconductors. *Chem. Mater.* **2019**, *31*, 1184–1195.
- (74) Xiao, Z.; Yan, Y. Progress in Theoretical Study of Metal Halide Perovskite Solar Cell Materials. *Adv. Energy Mater.* **2017**, *7*, 1701136.
- (75) McClure, E. T.; Ball, M. R.; Windl, W.; Woodward, P. M. $\text{Cs}_2\text{AgBiX}_6$ ($X = \text{Br}, \text{Cl}$): New Visible Light Absorbing, Lead-Free Halide Perovskite Semiconductors. *Chem. Mater.* **2016**, *28*, 1348–1354.
- (76) Tran, T. T.; Panella, J. R.; Chamorro, J. R.; Morey, J. R.; McQueen, T. M. Designing Indirect-Direct Bandgap Transitions in Double Perovskites. *Mater. Horiz.* **2017**, *4*, 688–693.
- (77) Zhang, P.; Yang, J.; Wei, S. H. Manipulation of Cation Combinations and Configurations of Halide Double Perovskites for Solar Cell Absorbers. *J. Mater. Chem. A* **2018**, *6*, 1809–1815.
- (78) Li, Z.; Napari, M.; Palgrave, R. G.; Abdi-Jalebi, M.; Andaji-Garmaroudi, Z.; Davies, D. W.; Laitinen, M.; Julin, J.; Richard, H.; Scanlon, D. O.; Walsh, A.; Hoye, R. L. Z. Bandgap Lowering in Mixed Alloys of $\text{Cs}_2\text{AgSb}_{1-x}\text{Bi}_x\text{Br}_6$ Double Perovskite Thin Films. *arXiv* **2020**, 2007.00388 [cond-mat.mtrl-sci].
- (79) Manna, D.; Das, T. K.; Yella, A. Tunable and Stable White Light Emission in Bi^{3+} -Alloyed $\text{Cs}_2\text{AgInCl}_6$ Double Perovskite Nanocrystals. *Chem. Mater.* **2019**, *31*, 10063–10070.
- (80) Majher, J. D.; Gray, M. B.; Strom, T. A.; Woodward, P. M. $\text{Cs}_2\text{NaBiCl}_6: \text{Mn}^{2+}$ - A New Orange-Red Halide Double Perovskite Phosphor. *Chem. Mater.* **2019**, *31*, 1738–1744.
- (81) Slavney, A. H.; Leppert, L.; Bartesaghi, D.; Gold-Parker, A.; Toney, M. F.; Savenije, T. J.; Neaton, J. B.; Karunadasa, H. I. Defect-Induced Band-Edge Reconstruction of a Bismuth-Halide Double Perovskite for Visible-Light Absorption. *J. Am. Chem. Soc.* **2017**, *139*, 5015–5018.
- (82) Yu, J.; Kong, J.; Hao, W.; Guo, X.; He, H.; Leow, W. R.; Liu, Z.; Cai, P.; Qian, G.; Li, S.; Chen, X.; Chen, X. Broadband Extrinsic Self-Trapped Exciton Emission in Sn-Doped 2D Lead-Halide Perovskites. *Adv. Mater.* **2018**, *31*, 1806385.
- (83) Li, S.; Luo, J.; Liu, J.; Tang, J. Self-Trapped Excitons in All-Inorganic Halide Perovskites: Fundamentals, Status, and Potential Applications. *J. Phys. Chem. Lett.* **2019**, *10*, 1999–2007.
- (84) Meng, W.; Wang, X.; Xiao, Z.; Wang, J.; Mitzi, D. B.; Yan, Y. Parity-Forbidden Transitions and Their Impact on the Optical Absorption Properties of Lead-Free Metal Halide Perovskites and Double Perovskites. *J. Phys. Chem. Lett.* **2017**, *8*, 2999–3007.
- (85) Luo, J.; Wang, X.; Li, S.; Liu, J.; Guo, Y.; Niu, G.; Yao, L.; Fu, Y.; Gao, L.; Dong, Q.; Zhao, C.; Leng, M.; Ma, F.; Liang, W.; Wang, L.; Jin, S.; Han, J.; Zhang, L.; Etheridge, J.; Wang, J.; Yan, Y.; Sargent, E. H.; Tang, J. Efficient and Stable Emission of Warm-White Light from Lead-Free Halide Double Perovskites. *Nature* **2018**, *563*, 541–545.
- (86) Hoard, J. L.; Goldstein, L. The Structure of Caesium Enneachlordarsenite, $\text{Cs}_3\text{As}_2\text{Cl}_9$. *J. Chem. Phys.* **1935**, *3*, 117–122.
- (87) Singh, A.; Boopathi, K. M.; Mohapatra, A.; Chen, Y. F.; Li, G.; Chu, C. W. Photovoltaic Performance of Vapor-Assisted Solution-Processed Layer Polymorph of $\text{Cs}_3\text{Sb}_2\text{I}_9$. *ACS Appl. Mater. Interfaces* **2018**, *10*, 2566–2573.
- (88) McCall, K. M.; Liu, Z.; Trimarchi, G.; Stoumpos, C. C.; Lin, W.; He, Y.; Hadar, I.; Kanatzidis, M. G.; Wessels, B. W. α -Particle Detection and Charge Transport Characteristics in the $\text{A}_3\text{M}_2\text{I}_9$ Defect Perovskites ($A = \text{Cs}, \text{Rb}$; $M = \text{Bi}, \text{Sb}$). *ACS Photonics* **2018**, *5*, 3748–3762.
- (89) Tran, T. T.; Pocs, C. A.; Zhang, Y.; Winiarski, M. J.; Sun, J.; Lee, M.; McQueen, T. M.; Nat, O. R. Spinon Excitations in the Quasi-1D $S = 1/2$ Chain $\text{Cs}_4\text{CuSb}_2\text{Cl}_{12}$. *Phys. Rev. B: Condens. Matter Mater. Phys.* **2020**, *101*, 235107.
- (90) Singhal, N.; Chakraborty, R.; Ghosh, P.; Nag, A. Low-Bandgap $\text{Cs}_4\text{CuSb}_2\text{Cl}_{12}$ Layered Double Perovskite: Synthesis, Reversible Thermal Changes, and Magnetic Interaction. *Chem. - Asian J.* **2018**, *13*, 2085–2092.
- (91) Cai, T.; Shi, W.; Hwang, S.; Kobbekaduwa, K.; Nagaoka, Y.; Yang, H.; Hills-Kimball, K.; Zhu, H.; Wang, J.; Wang, Z.; Liu, Y.; Su, D.; Gao, J.; Chen, O. Lead-Free $\text{Cs}_4\text{CuSb}_2\text{Cl}_{12}$ Layered Double Perovskite Nanocrystals. *J. Am. Chem. Soc.* **2020**, *142*, 11927–11936.
- (92) Wang, X. D.; Miao, N. H.; Liao, J. F.; Li, W. Q.; Xie, Y.; Chen, J.; Sun, Z. M.; Chen, H. Y.; Kuang, D.-B. The Top-down Synthesis of Single-Layered $\text{Cs}_4\text{CuSb}_2\text{Cl}_{12}$ Halide Perovskite Nanocrystals for Photoelectrochemical Application. *Nanoscale* **2019**, *11*, 5180–5187.
- (93) Vargas, B.; Torres-Cadena, R.; Reyes-Castillo, D. T.; Rodríguez-Hernández, J.; Gembicky, M.; Menéndez-Proupin, E.; Solis-Ibarra, D. Chemical Diversity in Lead-Free, Layered Double Perovskites: A Combined Experimental and Computational Approach. *Chem. Mater.* **2020**, *32*, 424–429.
- (94) Xu, J.; Liu, J.-B.; Wang, J.; Liu, B.-X.; Huang, B. Prediction of Novel p -Type Transparent Conductors in Layered Double Perovskites: A First-Principles Study. *Adv. Funct. Mater.* **2018**, *28*, 1800332.
- (95) Zhao, X. G.; Yang, J. H.; Fu, Y.; Yang, D.; Xu, Q.; Yu, L.; Wei, S. H.; Zhang, L. Design of Lead-Free Inorganic Halide Perovskites for Solar Cells via Cation-Transmutation. *J. Am. Chem. Soc.* **2017**, *139*, 2630–2638.

- (96) Han, D.; Zhang, T.; Chen, S. High-Throughput First-Principles Screening of Layered Magnetic Double Perovskites $\text{Cs}_4\text{MSb}_2\text{X}_{12}$ for Spintronic Applications. *J. Phys.: Condens. Matter* **2020**, *32*, 225705.
- (97) Yamatera, H.; Nakatsu, K. The Crystal Structure of $\text{Cs}_3\text{Fe}_2\text{Cl}_9$ and of $\text{Cs}_3\text{Sb}_2\text{Cl}_9$. *Bull. Chem. Soc. Japan* **1954**, *27*, 244.
- (98) Kamat, P. V.; Bisquert, J.; Buriak, J. Lead-Free Perovskite Solar Cells. *ACS Energy Lett.* **2017**, *2*, 904–905.
- (99) Sun, S.; Hartono, N. T. P.; Ren, Z. D.; Oviedo, F.; Buscemi, A. M.; Layurova, M.; Chen, D. X.; Ogunfunmi, T.; Thapa, J.; Ramasamy, S.; Settens, C.; DeCost, B. L.; Kusne, A. G.; Liu, Z.; Tian, S. I. P.; Peters, I. M.; Correa-Baena, J. P.; Buonassisi, T. Accelerated Development of Perovskite-Inspired Materials via High-Throughput Synthesis and Machine-Learning Diagnosis. *Joule* **2019**, *3*, 1437–1451.
- (100) Vargas, B.; Torres-Cadena, R.; Rodríguez-Hernández, J.; Gembicky, M.; Xie, H.; Jiménez-Mier, J.; Liu, Y.-S.; Menéndez-Proupin, E.; Dunbar, K. R.; Lopez, N.; Olalde-Velasco, P.; Solis-Ibarra, D. Optical, Electronic, and Magnetic Engineering of (111) Layered Halide Perovskites. *Chem. Mater.* **2018**, *30*, 5315–5321.
- (101) Vargas, B.; Reyes-Castillo, D. T.; Coutino-Gonzalez, E.; Ramos, C.; Sánchez-Aké, C.; Ciro, F.; Solis-Ibarra, D. Enhanced Luminescence and Mechanistic Studies on Layered Double Perovskite Phosphors: $\text{Cs}_4\text{Mn}_{1-x}\text{Cd}_x\text{Bi}_2\text{Cl}_{12}$. *Chem. Mater.* **2020**, DOI: 10.1021/acs.chemmater.0c03167.
- (102) Vargas, B.; Coutino-Gonzalez, E.; Ovalle-Encinia, O.; Sánchez-Aké, C.; Solis-Ibarra, D. Efficient Emission in Halide Layered Double Perovskites: The Role of Sb^{3+} Substitution in $\text{Cs}_4\text{Cd}_{1-x}\text{Mn}_x\text{Bi}_2\text{Cl}_{12}$ Phosphors. *Chem. Rxiv. Preprint* **2020** DOI: 10.26434/chemrxiv.12950804.v1.
- (103) Smith, M. D.; Crace, E. J.; Jaffe, A.; Karunadasa, H. I. The Diversity of Layered Halide Perovskites. *Annu. Rev. Mater. Res.* **2018**, *48*, 111–136.
- (104) Wang, X.; Meng, W.; Xiao, Z.; Wang, J.; Mitzi, D.; Yan, Y. First-Principles Understanding of the Electronic Band Structure of Copper-Antimony Halide Perovskite: The Effect of Magnetic Ordering. *arXiv* **2017**, 1707.09539 [cond-mat.mtrl-sci] <https://arxiv.org/abs/1707.09539>.
- (105) Holzapfel, N. P.; Majher, J. D.; Strom, T. A.; Moore, C. E.; Woodward, P. M. $\text{Cs}_4\text{Cd}_{1-x}\text{Mn}_x\text{Bi}_2\text{Cl}_{12}$ —A Vacancy-Ordered Halide Perovskite Phosphor with High-Efficiency Orange-Red Emission. *Chem. Mater.* **2020**, *32*, 3510–3516.
- (106) Volonakis, G.; Filip, M. R.; Haghighirad, A. A.; Sakai, N.; Wenger, B.; Snaith, H. J.; Giustino, F. Lead-Free Halide Double Perovskites via Heterovalent Substitution of Noble Metals. *J. Phys. Chem. Lett.* **2016**, *7*, 1254–1259.
- (107) Lin, Y.-P.; Hu, S.; Xia, B.; Fan, K.-Q.; Gong, L.-K.; Kong, J.-T.; Huang, X.-Y.; Xiao, Z.; Du, K.-Z. Material Design and Optoelectronic Properties of Three-Dimensional Quadruple Perovskite Halides. *J. Phys. Chem. Lett.* **2019**, *10*, 5219–5225.
- (108) Das Adhikari, S.; Guria, A. K.; Pradhan, N. Insights of Doping and the Photoluminescence Properties of Mn-Doped Perovskite Nanocrystals. *J. Phys. Chem. Lett.* **2019**, *10*, 2250–2257.
- (109) Xing, K.; Yuan, X.; Wang, Y.; Li, J.; Wang, Y.; Fan, Y.; Yuan, L.; Li, K.; Wu, Z.; Li, H.; Zhao, J. Improved Doping and Emission Efficiencies of Mn-Doped CsPbCl_3 Perovskite Nanocrystals via Nickel Chloride. *J. Phys. Chem. Lett.* **2019**, *10*, 4177–4184.
- (110) McCall, K. M.; Stoumpos, C. C.; Kostina, S. S.; Kanatzidis, M. G.; Wessels, B. W. Strong Electron-Phonon Coupling and Self-Trapped Excitons in the Defect Halide Perovskites $\text{A}_3\text{M}_2\text{I}_9$ ($\text{A} = \text{Cs}$, Rb ; $\text{M} = \text{Bi}$, Sb). *Chem. Mater.* **2017**, *29*, 4129–4145.
- (111) Wu, C.; Zhang, Q.; Liu, Y.; Luo, W.; Guo, X.; Huang, Z.; Ting, H.; Sun, W.; Zhong, X.; Wei, S.; Wang, S.; Chen, Z.; Xiao, L. The Dawn of Lead-Free Perovskite Solar Cell: Highly Stable Double Perovskite $\text{Cs}_2\text{AgBiBr}_6$ Film. *Adv. Sci.* **2018**, *5*, 1700759.
- (112) You, Y. M.; Liao, W. Q.; Zhao, D.; Ye, H. Y.; Zhang, Y.; Zhou, Q.; Niu, X.; Wang, J.; Li, P. F.; Fu, D. W.; Wang, Z.; Gao, S.; Yang, K.; Liu, J. M.; Li, J.; Yan, Y.; Xiong, R. G. An Organic-Inorganic Perovskite Ferroelectric with Large Piezoelectric Response. *Science* **2017**, *357*, 306–309.
- (113) Ye, H. Y.; Tang, Y. Y.; Li, P. F.; Liao, W. Q.; Gao, J. X.; Hua, X. N.; Cai, H.; Shi, P. P.; You, Y. M.; Xiong, R. G. Metal-Free Three-Dimensional Perovskite Ferroelectrics. *Science* **2018**, *361*, 151–155.
- (114) Yang, C. K.; Chen, W. N.; Ding, Y. T.; Wang, J.; Rao, Y.; Liao, W. Q.; Tang, Y. Y.; Li, P. F.; Wang, Z. X.; Xiong, R. G. The First 2D Homochiral Lead Iodide Perovskite Ferroelectrics: $[\text{R- and S-1-(4-Chlorophenyl)Ethylammonium}]_2\text{PbI}_4$. *Adv. Mater.* **2019**, *31*, 1808088.
- (115) Shrestha, S.; Fischer, R.; Matt, G. J.; Feldner, P.; Michel, T.; Osvet, A.; Levchuk, I.; Merle, B.; Golkar, S.; Chen, H.; Tedde, S. F.; Schmidt, O.; Hock, R.; Rühlig, M.; Göken, M.; Heiss, W.; Anton, G.; Brabec, C. J. High-Performance Direct Conversion X-Ray Detectors Based on Sintered Hybrid Lead Triiodide Perovskite Wafers. *Nat. Photonics* **2017**, *11*, 436–440.
- (116) Pan, W.; Wu, H.; Luo, J.; Deng, Z.; Ge, C.; Chen, C.; Jiang, X.; Yin, W.; Niu, G.; Zhu, L.; Yin, L.; Zhou, Y.; Xie, Q.; Ke, X.; et al. $\text{Cs}_2\text{AgBiBr}_6$ Single-Crystal X-Ray Detectors with a Low Detection Limit. *Nat. Photonics* **2017**, *11*, 726–732.
- (117) Liu, X.; Wang, S.; Long, P.; Li, L.; Peng, Y.; Xu, Z.; Han, S.; Sun, Z.; Hong, M.; Luo, J. Polarization-Driven Self-Powered Photodetection in a Single-Phase Biaxial Hybrid Perovskite Ferroelectric. *Angew. Chem., Int. Ed.* **2019**, *58*, 14504–14508.
- (118) Jayasankar, P. M.; Pathak, A. K.; Madhusudan, S. P.; Murali, S.; Batabyal, S. K. Double Perovskite $\text{Cs}_4\text{CuSb}_2\text{Cl}_{12}$ Microcrystalline Device for Cost Effective Photodetector Applications. *Mater. Lett.* **2020**, *263*, 127200.
- (119) Tang, G.; Xiao, Z.; Hosono, H.; Kamiya, T.; Fang, D.; Hong, J. Layered Halide Double Perovskites $\text{Cs}_{3+n}\text{M(II)}_n\text{Sb}_2\text{X}_{9+3n}$ ($\text{M} = \text{Sn}$, Ge) for Photovoltaic Applications. *J. Phys. Chem. Lett.* **2018**, *9*, 43–48.
- (120) Beaulac, R.; Archer, P. I.; Ochsenbein, S. T.; Gamelin, D. R. Mn^{2+} -Doped CdSe Quantum Dots: New Inorganic Materials for Spin-Electronics and Spin-Photonics. *Adv. Funct. Mater.* **2008**, *18*, 3873–3891.
- (121) Mir, W. J.; Sheikh, T.; Arfin, H.; Xia, Z.; Nag, A. Lanthanide Doping in Metal Halide Perovskite Nanocrystals: Spectral Shifting, Quantum Cutting and Optoelectronic Applications. *NPG Asia Mater.* **2020**, *12*, 9.
- (122) Chen, J.; Ma, J.; Guo, S. Q.; Chen, Y. M.; Zhao, Q.; Zhang, B. B.; Li, Z. Y.; Zhou, Y.; Hou, J.; Kuroiwa, Y.; Moriyoshi, C.; Bakr, O. M.; Zhang, J.; Sun, H. T. High-Efficiency Violet-Emitting All-Inorganic Perovskite Nanocrystals Enabled by Alkaline-Earth Metal Passivation. *Chem. Mater.* **2019**, *31*, 3974–3983.
- (123) Navas, J.; Sánchez-Coronilla, A.; Gallardo, J. J.; Cruz Hernández, N.; Piñero, J. C.; Alcántara, R.; Fernández-Lorenzo, C.; De Los Santos, D. M.; Aguilar, T.; Martín-Calleja, J. New insights into organic-inorganic hybrid perovskite $\text{CH}_3\text{NH}_3\text{PbI}_3$ nanoparticles. An experimental and theoretical study of doping in Pb^{2+} sites with Sn^{2+} , Sr^{2+} , Cd^{2+} and Ca^{2+} . *Nanoscale* **2015**, *7*, 6216–6229.
- (124) Zheng, W.; Huang, P.; Gong, Z.; Tu, D.; Xu, J.; Zou, Q.; Li, R.; You, W.; Bünzli, J. C. G.; Chen, X. Near-Infrared-Triggered Photon Upconversion Tuning in All-Inorganic Cesium Lead Halide Perovskite Quantum Dots. *Nat. Commun.* **2018**, *9*, 3462.
- (125) Milstein, T. J.; Kluherz, K. T.; Kroupa, D. M.; Erickson, C. S.; De Yoreo, J. J.; Gamelin, D. R. Anion Exchange and the Quantum-Cutting Energy Threshold in Ytterbium-Doped $\text{CsPb}(\text{Cl}_{1-x}\text{Br}_x)_3$ Perovskite Nanocrystals. *Nano Lett.* **2019**, *19*, 1931–1937.
- (126) Wu, Y.; Li, X.; Zeng, H. Highly Luminescent and Stable Halide Perovskite Nanocrystals. *ACS Energy Lett.* **2019**, *4*, 673–681.
- (127) Saidaminov, M. I.; Mohammed, O. F.; Bakr, O. M. Low-Dimensional-Networked Metal Halide Perovskites: The Next Big Thing. *ACS Energy Lett.* **2017**, *2*, 889–896.
- (128) Hu, S.; Xia, B.; Lin, Y. P.; Katase, T.; Fujioka, J.; Kamiya, T.; Hosono, H.; Du, K. Z.; Xiao, Z. P-Type Transparent Quadruple Perovskite Halide Conductors: Fact or Fiction? *Adv. Funct. Mater.* **2020**, *30*, 1909906.
- (129) Xu, J.; Liu, J. B.; Wang, J.; Liu, B. X.; Huang, B. Response to Comment on “Prediction of Novel p-Type Transparent Conductors

in Layered Double Perovskites: A First-Principles Study. *Adv. Funct. Mater.* **2020**, *30*, 2003149.

(130) Zhong, H.; Yang, M.; Tang, G.; Yuan, S. Type-II Lateral Heterostructures of Monolayer Halide Double Perovskites for Optoelectronic Applications. *ACS Energy Lett.* **2020**, *5*, 2275–2282.

(131) Huang, H.; Pradhan, B.; Hofkens, J.; Roeffaers, M. B. J.; Steele, J. A. Solar-Driven Metal Halide Perovskite Photocatalysis: Design, Stability, and Performance. *ACS Energy Lett.* **2020**, *5*, 1107–1123.

(132) Singh, S.; Chen, H.; Shahrokhi, S.; Wang, L. P.; Lin, C.-H.; Hu, L.; Guan, X.; Tricoli, A.; Xu, Z. J.; Wu, T. Hybrid Organic-Inorganic Materials and Composites for Photoelectrochemical Water Splitting. *ACS Energy Lett.* **2020**, *5*, 1487–1497.

(133) Jiang, Q.; Zhao, Y.; Zhang, X.; Yang, X.; Chen, Y.; Chu, Z.; Ye, Q.; Li, X.; Yin, Z.; You, J. Surface Passivation of Perovskite Film for Efficient Solar Cells. *Nat. Photonics* **2019**, *13*, 460–466.

(134) Wang, F.; Bai, S.; Tress, W.; Hagfeldt, A.; Gao, F. Defects Engineering for High-Performance Perovskite Solar Cells. *npj Flex. Electron.* **2018**, *2*, 22.

(135) Quintero-Bermudez, R.; Gold-Parker, A.; Proppe, A. H.; Munir, R.; Yang, Z.; Kelley, S. O.; Amassian, A.; Toney, M. F.; Sargent, E. H. Compositional and Orientational Control in Metal Halide Perovskites of Reduced Dimensionality. *Nat. Mater.* **2018**, *17*, 900–907.